Received: 23 March 2021 | Revised: 2 August 2021 | Accepted: 6 August 2021

DOI: 10.1002/glia.24076

GLIA

WILEY

RESEARCH ARTICLE

Astrocyte arborization enhances Ca^{2+} but not cAMP signaling plasticity

Samo Pirnat[1,2] | Mićo Božić[2] | Dorian Dolanc[2] | Anemari Horvat[1,2] | Petra Tavčar[2] | Nina Vardjan[1,2] | Alexei Verkhratsky[1,3,4] | Robert Zorec[1,2] | Matjaž Stenovec[1,2]

[1]Laboratory of Cell Engineering, Celica BIOMEDICAL, Ljubljana, Slovenia

[2]Laboratory of Neuroendocrinology-Molecular Cell Physiology, Faculty of Medicine, Institute of Pathophysiology, University of Ljubljana, Ljubljana, Slovenia

[3]Faculty of Biology, Medicine and Health, The University of Manchester, Manchester, UK

[4]Achucarro Center for Neuroscience, IKERBASQUE, Bilbao, Spain

Correspondence
Robert Zorec and Matjaž Stenovec, Laboratory of Neuroendocrinology-Molecular Cell Physiology, Faculty of Medicine, Institute of Pathophysiology, University of Ljubljana, Zaloška 4, 1000 Ljubljana, Slovenia.
Email: robert.zorec@mf.uni-lj.si and matjaz.stenovec@mf.uni-lj.si

Funding information
CipKeBip; European Cooperation in Science and Technology, Grant/Award Number: COST Action CA18133 (ERNEST); Javna Agencija za Raziskovalno Dejavnost RS, Grant/Award Numbers: J3-2523, J3-7605, J3-9266; Slovenian Research Agency, Grant/Award Numbers: CA18133, P3-0310

Abstract

The plasticity of astrocytes is fundamental for their principal function, maintaining homeostasis of the central nervous system throughout life, and is associated with diverse exposomal challenges. Here, we used cultured astrocytes to investigate at subcellular level basic cell processes under controlled environmental conditions. We compared astroglial functional and signaling plasticity in standard serum-containing growth medium, a condition mimicking pathologic conditions, and in medium without serum, favoring the acquisition of arborized morphology. Using opto−/electrophysiologic techniques, we examined cell viability, expression of astroglial markers, vesicle dynamics, and cytosolic Ca^{2+} and cAMP signaling. The results revealed altered vesicle dynamics in arborized astrocytes that was associated with increased resting $[Ca^{2+}]_i$ and increased subcellular heterogeneity in $[Ca^{2+}]_i$, whereas $[cAMP]_i$ subcellular dynamics remained stable in both cultures, indicating that cAMP signaling is less prone to plastic remodeling than Ca^{2+} signaling, possibly also in in vivo contexts.

KEYWORDS
astrocyte, Ca^{2+}, cAMP, confocal microscopy, electrophysiology, vesicles

1 | INTRODUCTION

Astrocytes are morphologically and functionally heterogeneous glial cells in the central nervous system. Immunolabeling of glial fibrillary acidic protein (GFAP) reveals major processes with finer cellular parts remaining unstained (Connor & Berkowitz, 1985) making astrocytes appear as stellate cells (Wolfes et al., 2017; Wolfes & Dean, 2018). Advanced visualization techniques revealed that astrocytes exhibit a more complex, spongioform structure (Benediktsson et al., 2005; Bushong et al., 2004). The morphological complexity of astrocytes arguably correlates with their extended homeostatic roles. Astroglia assist neuro- and synaptogenesis, provide substrates to neurons, regulate blood flow and the blood–brain barrier, control uptake and recycling of neurotransmitters, and produce and secrete various neurotrophic factors to regulate memory formation (Araque et al., 1999; Attwell et al., 2010; Augusto-Oliveira et al., 2020; Belanger

Samo Pirnat, Mićo Božić, and Dorian Dolanc share first authorship.

et al., 2011; Belanger & Magistretti, 2009; Chung et al., 2015; Verkhratsky & Nedergaard, 2018; Zorec et al., 2015). Astroglial dysfunction and atrophy are causally linked to the onset and progression of neurodevelopmental and neurodegenerative disorders (Pekny et al., 2016; Verkhratsky et al., 2019), changes in astrocyte structure and function have been associated with neuropsychiatric diseases as well (D'Adamo et al., 2021; Kim et al., 2018; Stenovec et al., 2020; Vardjan et al., 2016; Verkhratsky et al., 2014). In addition, lesions to the central nervous system, irrespective of their nature, instigate complex molecular, functional, and morphological remodeling of astrocytes, known as reactive astrogliosis linked to an astrocyte defensive function (Escartin et al., 2021; Verkhratsky et al., 2017).

Defined environmental conditions are required to monitor astrocytic basic signaling mechanisms in normal and pathologic contexts, and an in vitro culture model appears to be an ideal solution. However, as the exact composition of interstitial solution surrounding single cells in vivo is unknown, the composition of cell culture media is an approximation at best. In this study, we used two cell culture systems with astrocytes exhibiting different morphological characteristics. The first, classic system requires supplementation of culture medium with fetal bovine serum (DMEM+ medium) (McCarthy & de Vellis, 1980), generating astrocytes with a polygonal fibroblast-like morphology; we designated these cells as DMEM+ astrocytes. Although beneficial for cell survival and proliferation (Aswad et al., 2016; Jayme et al., 1997), the composition of serum cannot be precisely determined because serum batches are prone to substantial variability; this is a challenge that cannot be controlled (Codeluppi et al., 2011; Zheng et al., 2006). Moreover, astrocytes in vivo are not in contact with serum, because many serum components do not cross the blood–brain barrier except in pathologic conditions (Schachtrup et al., 2010). Exposure to serum alters the astrocyte transcriptome (Foo et al., 2011) therefore DMEM+ astrocytes apparently constitute a mixture of proliferating and possibly reactive astrocytes (Du et al., 2010; Zamanian et al., 2012; Zhang et al., 2016). To alleviate some of the drawbacks of the DMEM+ culture model, several modifications were proposed (Fischer et al., 1982; Morrison & de Vellis, 1981). Addition of heparin-binding epidermal growth factor (hbEGF) (Foo et al., 2011) promotes the formation of astrocytic processes (Placone et al., 2015; Puschmann et al., 2013). Similarly, astrocytes grown in serum-free medium develop thin processes with glutamate-induced Ca^{2+} fluctuations (Morita et al., 2003). However, cultured arborized astrocytes lacked the spontaneous Ca^{2+} fluctuations observed in brain slices (Foo et al., 2011; Nett et al., 2002). Immunopanning, an alternative method that utilizes immunoprecipitation of cells by an antibody immobilized to a solid surface, is a lengthy procedure that potentially selects only a subpopulation of astrocytes (Foo et al., 2011). A recent change to the original protocol, referred to as the low-cost easy stellate astrocyte method, produces process-bearing arborized (also known as "AWESAM" or NB+) astrocytes that acquire a more realistic morphology, have a distinct (compared with DMEM+ astrocytes) gene expression profile, and generate Ca^{2+} signals similar to astrocytes co-cultured with other glia and neurons (Wolfes et al., 2017; Wolfes & Dean, 2018).

To analyze the functional plasticity of astroglia, we studied astrocytes grown in serum-containing medium (DMEM+) and serum-free medium (NB+). We examined cell viability, the expression of astrocyte-specific markers, intracellular vesicle mobility, exo−/endocytotic activity as well as spontaneous and evoked cytoplasmic Ca^{2+} ($[Ca^{2+}]_i$) and 3′,5′-cyclic adenosine monophosphate ($[cAMP]_i$) signaling. We found that NB+ astrocytes, when compared with DMEM+ astrocytes, exhibit an increase in subcellular heterogeneity in Ca^{2+} signaling, but not in cAMP signaling, indicating distinct subcellular plasticity of these two signaling systems.

2 | MATERIALS AND METHODS

2.1 | Cell cultures

Primary astrocyte cultures were prepared from neocortices of 2- to 3-day-old female Wistar rats (obtained from the Medical Experimental Centre at the Institute of Pathology, University of Ljubljana, Slovenia) as previously described (Schwartz & Wilson, 1992); the method was based on the original McCarthy and de Vellis protocol (McCarthy & de Vellis, 1980). Animal handling was in accordance with the European and Slovenian legislation (Official Gazette of the RS 38/13; UVHVVR, no. U34401-47/2014/7). Cells were grown in DMEM+ medium (high-glucose [25 mM] Dulbecco's modified Eagle's medium (DMEM) supplemented with 10% fetal bovine serum, 1 mM sodium pyruvate, 2 mM L-glutamine, and 5 U/ml penicillin, 5 μg/ml streptomycin) in an atmosphere of 5% CO_2/95% air. To purify isolated cells, sub-confluent cultures were shaken three times at 225 rpm overnight with subsequent medium change. Before the experiments, cells were trypsinized, sub-cultured (50 μl of cell suspension) onto poly-L-lysine-coated coverslips and left for 20 min at 37°C in an atmosphere of 5% CO_2/95% air to allow the cells to attach to the coverslip surface. Coverslips were then further maintained in either DMEM+ medium or washed twice with pure Neurobasal medium (NB; Thermo Fisher Scientific, Waltham, MA, USA) and from then on maintained in NB+ medium (NB complemented with B27 supplement (2%; Thermo Fisher Scientific), hbEGF (5 ng/ml), GlutaMAX (2 mM; Thermo Fisher Scientific), 5 U/ml penicillin, 5 μg/ml streptomycin). A subset of experiments was conducted in human astrocytes (Innoprot, P10254, Derio, Spain, EU) that were cultured in the same growth media as rat cortical astrocytes. Rat cells grown in DMEM+ or NB+ medium are designated as DMEM+ or NB+ astrocytes, whereas human cells cultured in DMEM+ medium as hDMEM+, respectively. Unless stated otherwise, all chemicals were purchased from Merck (Darmstadt, Germany) and were of the highest purity grade available.

2.2 | Preparation, staining and imaging of acute rat brain slices

Acute whole brain slices were prepared from 8- to 12-week old male Wistar rats. Animals were sacrificed by exposure to 100% CO_2 for

~5 min and immediately decapitated. The brains were carefully removed and immersed in ice-cold slicing artificial cerebrospinal fluid (aCSF) solution containing (in mM): 123 NaCl, 2.5 KCl, 1.3 NaH_2PO_4, 26.2 $NaHCO_3$, 10 D-glucose, 4 $MgCl_2$ and 0.5 $CaCl_2$ at pH 7.4 (oxigenized with 95% O_2, 5% CO_2) and osmolality of ~300 mOsm, measured with Osmomat 030 (Gonotech GmbH, Germany). The cerebellum and frontal section (approximately one-third) of the brain were cut with a scalpel blade, and the frontal aspect of the brain was glued onto the cutting table of a vibratome (VT1000 S, Leica Biosystems, Wetzlar, Germany). Coronal slices with a thickness of 250 μm were cut and submerged in ice-cold slicing aCSF throughout the sectioning process. Then, the slices were stained with astrocyte specific fluorescent marker sulforhodamine 101 (SR101; 1 μM) at 35°C for 20 min and left to recover for at least 40 min in recovery aCSF solution containing (in mM): 123 NaCl, 2.5 KCl, 1.3 NaH_2PO_4, 26.2 $NaHCO_3$, 10 D-glucose, 2.5 $MgCl_2$ and 1 $CaCl_2$ at pH 7.4 (oxigenized with 95% O_2, 5% CO_2) and ~ 300 mOsm.

Before being loaded with the Ca^{2+} indicator Fluo-4 AM, that specifically labels astrocytes in vivo (Hirase et al., 2004) and in situ (Dallwig & Deitmer, 2002), slices were incubated with 0.0013% Kolliphor^{EL}, according to the previously published protocol (Dawitz et al., 2011). After that, slices were loaded for 1.5 h at room temperature with 15 μM Fluo-4 AM and 0.05% pluronic acid (Molecular Probes, Eugene, OR, USA) in experimental aCSF solution containing (in mM): 123 NaCl, 2.5 KCl, 1.3 NaH_2PO_4, 26.2 $NaHCO_3$, 10 D-glucose, 1.3 $MgCl_2$ and 2.5 $CaCl_2$ at pH 7.4 (oxigenized with 95% O_2, 5% CO_2) and ~ 300 mOsm. Finally, slices were washed to remove Fluo-4 AM and incubated for 1 h at room temperature in dye-free experimental aCSF prior to experiments.

Acute brain slices were examined with a two-photon microscope Zeiss LSM 7 *MP* (Carl Zeiss, Germany) using water objective Plan-Apochromat 20×/1.0 DIC (Carl Zeiss, Germany) and 800 nm (Fluo-4 AM) and 900 nm (SR101) Ti:Sapphire laser (Chameleon Coherent, Santa Clara, California, USA) excitation coupled with 500–550 nm (Fluo4-AM) and 575–610 nm (SR101) band-pass emission filters. Cortical brain tissue astrocytes were perfusion-stimulated at the rate of 1 ml/min with 10 μM NA. Time-lapse images were acquired every second. Fluo-4 AM fluorescence intensities were quantified within a region of interest for individual astrocytes and expressed as the relative change in fluorescence: $\Delta F/F_0 = (F - F_0)/F_0$, where F_0 is the fluorescence level at the start of the experiment.

2.3 | Astrocyte viability and analysis

The viability of astrocytes (DMEM+ and NB+) in both cultures was determined at day 1 and day 7 after cell plating using a Live/Dead Viability/Cytotoxicity Kit for Mammalian Cells (Thermo Fisher Scientific) as described in Goncalves et al., 2008. In a subset of experiments, astrocytes from both cultures were transferred into the recording chamber and supplied with 400 μl of extracellular solution (ECS) containing 4 μM FM4-64 (T3166; Thermo Fisher Scientific) to stain the plasma membrane and vesicles internalized during endocytosis (Rigal et al., 2015).

2.4 | Immunocytochemistry and image analysis

Immunocytochemical staining of astrocytes was performed as described previously (Stenovec et al., 2016). The following primary and secondary antibodies were used: mouse monoclonal anti-nestin (dilution 1:400; ab11306, Abcam), mouse monoclonal anti-GFAP (dilution 1:500; G3893, Merck), rabbit polyclonal anti-MFGE8 (dilution 1:250; sc33546, Santa Cruz Biotechnology, Dallas, TX, USA), and anti-mouse or anti-rabbit antibodies conjugated to Alexa Fluor 488 or 546 (1:600; Thermo Fisher Scientific). The counts of immunolabeled GFAP- and/or MFGE8-positive astrocytes were obtained as described in the section on Astrocyte viability and analysis.

2.5 | Visualization of vesicles and analysis of mobility

Astrocytes were preloaded at 37°C overnight with 10 μM Dextran conjugated to Alexa Fluor 488 (Dex488; MW 10,000 Da, D22910, Thermo Fisher Scientific) in the respective culture media (DMEM+ and NB+ media). Mobility of individual dextran-laden endocytotic vesicles was analyzed in time-lapse images acquired every 485 ms for 1 min before and 2 min after stimulation with 100 μM ATP in exported tiff files by ParticleTR software (Celica, Ljubljana, Slovenia) as described previously (Lasic et al., 2020).

2.6 | Membrane capacitance measurements

Individual exo−/endocytotic events were detected in membrane capacitance traces as discrete up−/downward steps that reflect the sudden addition (exocytosis) or removal (endocytosis) of the vesicle membrane to/from the patch of cell membrane (Neher & Marty, 1982). Cell-attached membrane capacitance measurements were performed as previously described (Bozic et al., 2020; Rituper et al., 2013). Only recordings that contained at least a net 3 min of low-noise recording time were included in the analysis. The low background noise in the cell-attached configuration enables the detection of single exo−/endocytotic vesicles interacting with the plasmalemma with a diameter as small as 35 to 60 nm (Gucek et al., 2016; Kreft & Zorec, 1997; Rituper et al., 2013).

Individual exo−/endocytotic events were manually detected in the CellAn program (Celica BIOMEDICAL) written for MATLAB. The given event was accepted if: (i) the signal-to-noise ratio was at least 3 to 1 and (ii) it was not a result of crosstalk from the current (I) signal due to spontaneous single channel activity or temporary seal instability (Henkel et al., 2000; Rituper et al., 2013). The given event was designated either reversible (reversible exo−/endocytosis) if an initial up−/downward step was followed by a subsequent step of similar amplitude and opposite direction within 15 s, or irreversible (full exo−/endocytosis) if no similar subsequent step occurred within 15 s (Bozic et al., 2020; Lasic et al., 2016; Lasic et al., 2017). Vesicle capacitance (C_v) was calculated with the formula, $C_v = [(Re^2 + Im^2)/Im]/\omega$, where ω denotes angular frequency: $\omega = 2\pi f$ (Lindau, 1991). Given

that membrane capacitance is proportional to the cell membrane surface area, the vesicle surface and thus diameter (d) can be determined by $C_v = C_{spec}\pi d^2$,where C_{spec} is the specific membrane capacitance ($C_{spec} = 10\ fF/\mu m^2$) (Trachtenberg et al., 1972) and assuming spherical vesicle geometry. Reversible exo−/endocytotic events that displayed measurable projections to Re were used to calculate fusion pore conductance, $G_p = (Re^2 + Im^2)/Re$, from which the fusion pore diameter was calculated with the equation: $G_p = (\pi r^2)/(\rho\lambda)$ where ρ is estimated saline resistivity (100 Ωcm), and r and λ are the estimated fusion pore radius and length (15 nm), respectively (Kabaso et al., 2013; Lindau, 1991; Spruce et al., 1990).

2.7 | Calcium imaging and analysis

2.7.1 | Fura-2 measurements

Ninety-six hours after sub-culturing, astrocyte-loaded coverslips were incubated for 30 min at room temperature in 1 ml of culture medium (DMEM+ or NB+ medium) supplemented with 4 μM Fura-2 AM, a cell-permeant ratiometric fluorescent calcium indicator. Cells were washed twice with ECS (pH 7.3) (Bozic et al., 2020) and incubated in ECS for an additional 30 min at room temperature. Thereafter, coverslips were washed twice, immersed in 400 μl of ECS and mounted in the recording chamber on a fluorescence microscope Axio Observer.A1 (Zeiss). Cells were observed by an EC Plan Neofluar oil immersion 40×/NA 1.3 objective. Fura-2 was excited by monochromator Polychrome V (Till Photonics, Graefelfing, Germany) using filter set 21 HE (Zeiss), and emission fluorescence was band-pass filtered at 420–600 nm and captured by a CCD camera Luca S (Andor Technology, Belfast, UK). During the measurements, cells were sequentially excited with 340 and 380 nm (100 ms exposure time with 10 ms delay between the excitation wavelengths) at 1-s intervals for a total of 10 min. Cell were first monitored for 5 min and then stimulated with 100 μM ATP to record ATP-evoked changes in $[Ca^{2+}]_i$ for an additional 5 min. For analysis, regions of interest (ROIs; delimiting cell soma) were drawn, and the ratio of fluorescence intensities (F_{340}/F_{380}) recorded with Till Photonics Live Acquisition software was calculated and corrected for background fluorescence.

Two-point calibration to determine F_{340}/F_{380} ratios at minimum and saturating $[Ca^{2+}]_i$ was independently performed in each culture. In brief, Fura-2 AM-loaded cells were incubated at room temperature for 10 min in MIN (138 mM NaCl, 5 mM KCl, 1 mM $MgCl_2$, 1 mM EGTA, 10 μM ionomycin, 10 mM HEPES/NaOH, pH 7.3) and MAX (128 mM NaCl, 5 mM KCl, 10 mM $CaCl_2$, 1 mM $MgCl_2$, 10 μM ionomycin, 10 mM HEPES/NaOH, pH 7.3) solution to obtain R_{max} (F340/F380 fluorescence ratio in MAX solution), R_{min} (F340/F380 fluorescence ratio in MIN solution), F_{max} (F380 in MAX solution) and F_{min} (F380 in MIN solution) coefficients. $[Ca^{2+}]_i$ was calculated using the formula $[Ca^{2+}]_i = K_d \times ((R - R_{min})/(R_{max} - R)) \times (F_{min}/F_{max})$. The K_d values used in the calculations was 225 nM (Dong et al., 2017). Baseline (b) $[Ca^{2+}]_i$ concentration was calculated as the average $[Ca^{2+}]_i$ of the first 300 recordings (before the addition of ATP). The highest $[Ca^{2+}]_i$ value measured in a given sequence was set as the peak (p) $[Ca^{2+}]_i$ value, whereas the area under the curve (S) was calculated using the trapezoidal rule for the first 120 data points (120 s) after ATP stimulation.

2.7.2 | Fluo-4 measurements

Fluo-4 AM (5 μM; Thermo Fisher Scientific)-loaded cells (similar preparation steps as for Fura-2 measurements described above) were mounted onto the LSM 780 confocal microscope and observed either with a Plan-Apochromat 20×/NA 0.8 objective (Zeiss; for measuring global calcium activity) or a Plan-Apochromat 63×/NA 1.4 oil immersion objective (Zeiss; for measuring calcium activity in microdomains). Fluo-4 was excited by a 488-nm argon laser line, and emission fluorescence was filtered with a 495–565 nm band-pass filter. Time-lapse images were acquired every second for 5 min before and 10 min after the bolus addition of ATP, which reached a final concentration of 100 μM. Baseline fluorescence was set to equal the average fluorescence intensity of the first 300 recordings (pre-ATP stimulation).

2.7.3 | Analysis of calcium oscillations

$[Ca^{2+}]_i$ dynamics was classified into one of three categories: transient, sustained (persistent), or oscillatory responses (Yoshida et al., 2005). To further characterize ATP-evoked oscillatory responses in DMEM+ and NB+ astrocytes, the oscillation period (up to a maximum period of 30 s) was determined by using the WAVOS toolkit (Harang et al., 2012) in MATLAB. The continuous wavelet transform method utilizing the Morlet wavelet (Szekely et al., 2009) was used.

2.8 | cAMP imaging and analysis

2.8.1 | Epac1-camps measurements and analysis

Astrocytes were transfected with plasmid encoding Epac1-camps (0.8 μg/μl) (Nikolaev et al., 2004) using FuGENE 6 Transfection Reagent (Promega Corporation, Madison, WI, USA) and imaged 24–48 h after transfection. Astrocyte-loaded coverslips were mounted into the chamber in a confocal microscope (LSM 780, Zeiss), and imaged by a Plan-Apochromat air objective 20×/NA 0.8 or a Plan-Apochromat 63×/NA 1.4 oil immersion objective. Epac1-camps was excited by a 458 nm argon laser line, and two-channel (cyan fluorescent protein [CFP] and yellow fluorescent protein [YFP]) images were acquired by a gallium arsenide phosphide (GaAsP) detector. CFP and YFP emission spectra were band-pass filtered from 473–499 nm and 508–534 nm, respectively. Time-lapse CFP and YFP images were acquired every 2 s for 2 min before and 5 min after the bolus addition of noradrenaline (NA), which reached a final concentration of 100 μM. For analysis, changes in CFP and YFP fluorescence intensities were extracted from DMEM+ and NB+ astrocytes by ZEN 2010B software (Zeiss) within the ROIs of interest that encompassed individual cells. After subtracting the background fluorescence (mean + 3 × *SD*) from

the CFP and YFP channels in Excel (Microsoft, Redmond, WA, USA), we calculated the fluorescence resonance energy transfer (FRET) signal as the ratio of CFP to YFP fluorescence. An increase in $[cAMP]_i$ is thus reflected as an increase in the FRET signal.

To estimate the time constant (τ) of the NA-evoked increase in $[cAMP]_i$ in DMEM+ and NB+ astrocytes, we fitted a single-exponential increase to maximum function ($f = y_0 + a \times (1 - \exp[-b \times x])$ to time-dependent changes in CFP/YFP fluorescence ratio using SigmaPlot (Systat Software, San Jose, CA, USA); $\tau = 1/b$. The maximal amplitude (a_{max}) of the $[cAMP]_i$ increase was calculated as a quotient of the CFP/YFP fluorescence ratio at the end of NA stimulation (averaged over the last 20 s) versus the resting CFP/YFP fluorescence ratio before application of NA (averaged over the last 20 s) and expressed as % increase.

To characterize microdomains of $[cAMP]_i$ in individual astrocytes, MATLAB was used to draw linear paths in a perpendicular direction from the edge of the cell nucleus toward the periphery/processes and equidistantly placed circular ROIs ($2r = 2$ μm) along these paths. The mean CFP/YFP ratio within individual ROIs was calculated after correction of background fluorescence. To estimate time-dependent changes in $[cAMP]_i$ within a given microdomain (ROI), the entire time series of CFP and YFP images was processed (either 120 or 420 s). To estimate the resting level of $[cAMP]_i$ (CFP/YFP ratio), we averaged data points gathered in the first 30 s within an individual ROI (the total recording time of 420 s with 100 μM NA added at 120 s). Similarly, to estimate the stimulated level of $[cAMP]_i$, we averaged data from the last 30 s within an individual ROI after addition of 100 μM NA to astrocytes. All CFP/YFP ratio values calculated in individual cells were normalized using the following function $x' = (x - x_{min})/(x_{max} - x_{min})$.

2.8.2 | cAMP accumulation assay by AlphaScreen

DMEM+ and NB+ astrocytes growing on multiwell plates were non-enzymatically detached with dissociation solution. cAMP accumulation was measured in nonstimulated cells (3000 cells per well, each sample in triplicate) by the AlphaScreen cAMP assay kit according to the manufacturer's protocol in 384-well OptiPlate microplates (PerkinElmer Life Sciences, Waltham, MA) using the EnSpire Reader equipped with Alpha technology (PerkinElmer Life Sciences, Waltham, MA). The values of the ALPHA signal (in counts per second [cps]) were converted into cAMP production values by interpolating from a standard curve run in parallel using GraphPad Prism software (GraphPad, San Diego, CA, USA), and fitted by the four-parameter logistic Equation ($F = \min + (\max\text{-}\min)/(1 + [x/EC_{50}]^{-\text{Hill slope}})$), with weighting of $1/Y^2$. The cAMP concentration produced during 30 min in 25 μl of suspension containing 3000 cells was used to estimate the average cell cAMP production rate (pM cAMP produced per cell per min) using Excel (Microsoft).

2.9 | Statistical analysis

Data analysis was performed using SigmaPlot (Systat Software, San Jose, CA, USA) and Excel (Microsoft). Measured parameters are presented as means ± *SEM* or median values and interquartile range (third quartile [Q3]–first quartile [Q1]). Unless stated otherwise, Student's *t*-test and Mann–Whitney *U*-test were used to determine statistical significance; $p < .05$ was considered significant.

3 | RESULTS

3.1 | Morphology, viability, and astroglial markers in DMEM+ and NB+ astrocytes

Typical astrocyte morphology in different culture media was visualized using membrane styryl dye FM4-64 (Figure 1a,b). Cell morphology was quantified in both cultures by the cell shape factor ($CSF = 4 \times \pi \times S/p^2$; frequency distributions are displayed in Figure 1c,d), where S represents the surface area and p is the cell perimeter (Vardjan et al., 2014). CSF was significantly lower in NB+ (0.35 ± 0.03, n = 63) than in DMEM+ astrocytes (0.53 ± 0.03; $p < .001$, n = 71, Mann–Whitney *U*-test), indicating the prevalence of cells with arborized structure in the NB+ culture. The cell viability assay (Figure S1a) revealed >96% survival rate of astrocytes from both cultures (Figure S1b). Purified postnatal astrocytes cultured in media with hbEGF, a mitogenic factor, display an ability to proliferate and divide once every 3 days, whereas DMEM+ astrocytes divide faster, every 1.4 days (Foo et al., 2011). Hence, we examined whether nestin, a marker of progenitor cells (Bernal & Arranz, 2018) is less expressed in NB+ astrocytes. The relative percentage of nestin-positive cells was significantly lower ($p < .001$) in NB+ versus DMEM+ astrocytes (Figure S1c,d). The expression of GFAP, a common astrocytic marker, and milk fat globule-EGF factor 8 protein (MFGE8), a marker of telencephalon astrocytes (Zeisel et al., 2018), was different between the cultures. Whereas all DMEM+ and NB+ astrocytes were MFGE8-positive, the relative fraction of double, GFAP-, and MFGE8-positive cells was lower ($p < .001$) in NB+ astrocytes (Figure S2a–c). Astrocytes in both cultures thus exhibit different cell morphology and GFAP expression.

3.2 | Mobility of endocytotic vesicles is attenuated in NB+ astrocytes

Vesicle traffic in astrocytes plays a pivotal role in regulated exocytosis and in the uptake of extracellular molecules (Potokar et al., 2013; Verkhratsky et al., 2016). Detailed examination of dextran-laden vesicles (Figure 1e,f) revealed their attenuated mobility in NB+ versus DMEM+ astrocytes ($p < .001$; Figure 1g–l). As the mobility of endocytotic vesicles depends on cytosolic Ca^{2+} (Potokar et al., 2008), we stimulated cells in both cultures with 100 μM ATP triggering Ca^{2+} signaling (Pangrsic et al., 2006; Verkhratsky et al., 2020). Stimulation with ATP significantly suppressed ($p < .001$) vesicle mobility as indicated by a decrease in track length (TL; Figure S3a,b) and maximal displacement (MD; Figure S3c,d). In addition, purinergic receptor activation exerted greater impact on vesicle mobility in DMEM+ than

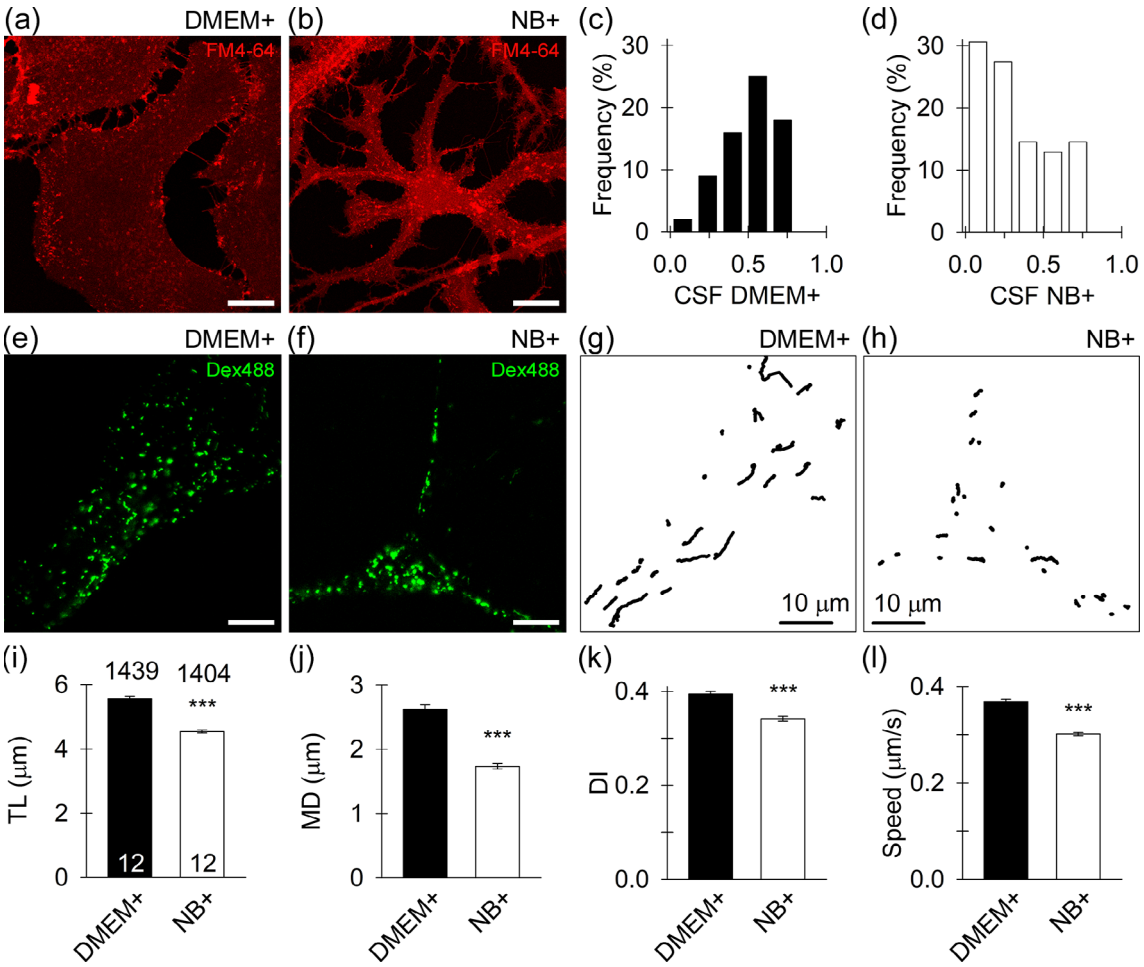

FIGURE 1 Attenuated spontaneous mobility of dextran-positive vesicles in NB+ astrocytes. (a), (b) confocal micrographs of morphologically distinct nonarborized serum (a; DMEM+) and arborized (b; NB+) astrocytes labeled with membrane styryl dye FM4-64. (c), (d) the relative frequency distribution (in %) of the cell shape factor ($=4 \times \pi \times S/p^2$, where S represents the surface area and p the cell perimeter) values calculated in DMEM+ astrocytes (c) and NB+ astrocytes (d). e, f confocal micrographs of DMEM+ astrocytes (e) and NB+ astrocytes (f) with numerous endocytotic vesicles that internalized fluorescent dextran (Dex488, green). Scale bars, 10 μm. (g), (h) trajectories of Dex488-positive vesicles (n = 30) reconstructed for a 15 s epoch in DMEM+ astrocytes (g) and NB+ astrocytes (h). Note the less elongated vesicle tracks in NB+ astrocyte. Scale bars, 10 μm. (i), (j), (k), (l) track length (TL; (i)), maximal displacement (MD; (j)), directionality index (DI; (k)), and speed (l) of Dex488-positive vesicles in DMEM+ and NB+ astrocytes. Note that all parameters of vesicle mobility (TL, MD, DI, and speed), are diminished in NB+ astrocytes. The numbers at the top and at the bottom of the bars (mean ± SEM) indicate the number of vesicles and cells analyzed, respectively. ***$p < .001$ (Mann–Whitney *U*-test)

NB+ astrocytes, as revealed by a larger relative decrease in track length and maximal displacement within the first poststimulation minute; 44% versus 25%, and 71% versus 57% (DMEM+ versus NB+), respectively. Notably, the directionality index (DI) also decreased in astrocytes from both cultures; the decrease was larger in NB+ astrocytes ($p < .001$; Figure S3e,f).

3.3 | Elementary exo−/endocytosis events are similar in astrocytes from both cultures

To characterize astroglial elementary exo−/endocytosis, we monitored membrane capacitance (C_m), a parameter linearly related to the membrane area (Neher & Marty, 1982; Zorec et al., 1991). In total, we recorded from 62 DMEM+ and 48 NB+ astrocytes with an average recording time of 16.3 ± 0.4 min and cumulative recording time of 29 h and 52 min, respectively. In agreement with previous reports, we observed distinct types of elementary exo−/endocytosis (Bozic et al., 2020; Gucek et al., 2016; Lasic et al., 2016; Lasic et al., 2017). The appearance of an upward or a downward step in C_m was interpreted either as a complete merger (full exocytosis; Figure 2a-i) or as a complete fission of a vesicle from the plasmalemma (full endocytosis; Figure 2a-ii), respectively. If a step in C_m was followed by a similar step in the opposite direction within 15 s, we regarded such an event as a reversible vesicle exo−/endocytosis (Figure 2a-iii,iv) (Bozic et al., 2020; Lasic et al., 2016; Lasic et al., 2017). In occasional bursting events, (Lasic et al., 2016; Lasic et al., 2017) we calculated the average amplitude in C_m and the dwell time of the first and last flicker (short

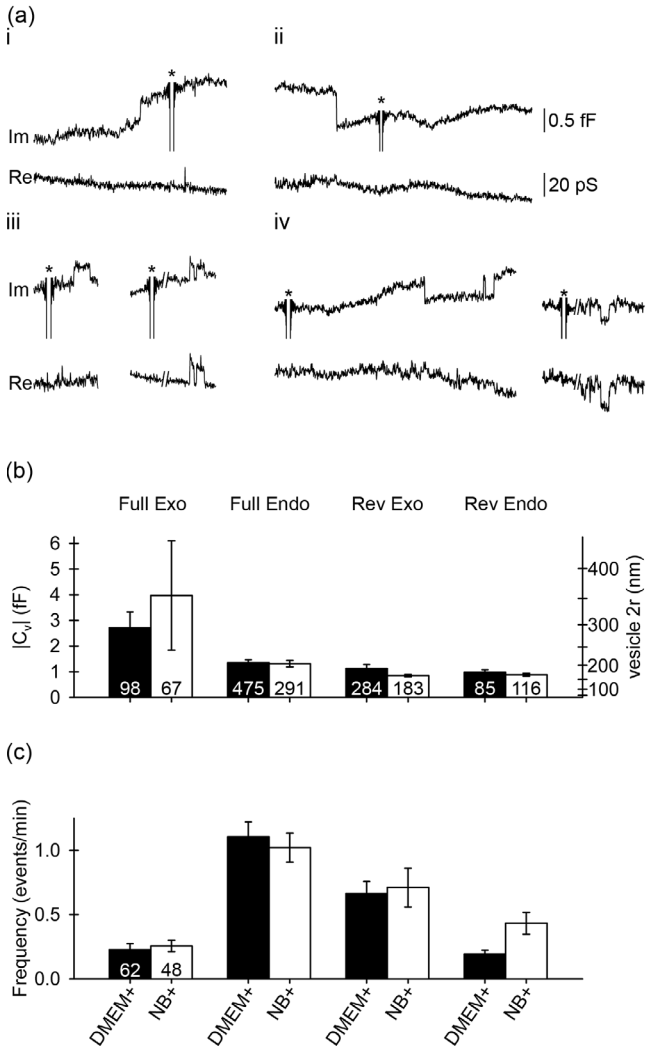

FIGURE 2 The size and frequency of elementary exo−/endocytotic events are similar in DMEM+ and NB+ astrocytes. (a) Representative examples of different types of exo−/endocytotic events recorded as discrete upward/downward steps in the imaginary (Im; proportional to membrane capacitance, C_m) and real (Re) parts of the admittance signals representing full exocytosis (i), full endocytosis (ii), reversible exocytosis (iii), and reversible endocytosis (iv). All elementary events were obtained in NB+ astrocytes and are similar to events obtained in serum astrocytes, as reported (Lasic et al., 2020). Asterisks denote calibration pulses. The projection from the Im to the Re signal (iii, right and iv, right) enabled calculation of fusion pore conductance (G_p) and the fusion pore diameter (2r) as described in Figure S4 (see Section 2). (b,c) vesicle capacitance (C_v), vesicle diameter (2r; (b)) and frequency (c) of different types of exo−/endocytotic events: Full exocytosis (full Exo; [a-i]), full endocytosis (full Endo; [a-ii]), reversible exocytosis (rev Exo; [a-iii]), reversible endocytosis (rev Endo; [a-iv]) in resting serum (DMEM+) and arborized (NB+) astrocytes. Numbers at the bottom of the bars indicate the number of vesicles (b) and cells (c) analyzed

step-like change in C_m) in the burst and pooled these data together with reversible exo−/endocytotic events (Bozic et al., 2020).

Vesicle capacitance (C_v) and diameter (d, calculated by assuming spherical vesicle geometry and the specific membrane capacitance of 10 fF/μm^2) (Trachtenberg et al., 1972) of exo−/endocytotic vesicles was similar in both cultures (Figure 2b; Table S1), consistent with previously published results (Lasic et al., 2017). In addition, all events occurred with a comparable frequency in DMEM+ and NB+ astrocytes (Figure 2c; Table S1).

Reversible step-like changes in the I_m admittance signal displaying projections to the Re admittance signal (Figure 2a-iii, right traces; Figure 2a-iv, right traces; Figure S4a) were recorded as previously described (Gucek et al., 2016). These changes were interpreted as transient openings of a relatively narrow fusion pore, which acted as an additional resistive element, enabling the estimation of fusion pore conductance (G_p), a parameter related to fusion pore diameter (see Materials and methods (Kabaso et al., 2013; Lindau, 1991; Spruce et al., 1990)). In reversible exocytotic events, the G_p was larger in NB+ versus DMEM+ astrocytes: 41 pS (Q1, 32; Q3, 51; n = 89 events; 26 cells with at least one applicable event) versus 27 pS (Q1, 20; Q3, 49; n = 174 events; 44 cells with at least one applicable event; $p < .001$), respectively (Figure S4b). In addition, the dwell time of all reversible exocytotic events was prolonged in NB+ astrocytes: 0.09 s (Q1, 0.04; Q3, 0.36; n = 183 events; 37 cells with at least one applicable event) versus 0.05 s (Q1, 0.03; Q3, 0.26; n = 284 events; 52 cells with at least one applicable event; $p = .02$; Figure S4c). However, both parameters were comparable in reversible endocytotic events. The G_p was 42 pS (Q1, 32; Q3, 63; n = 59 events; 19 cells with at least one applicable event) versus 46 pS (Q1, 32; Q3, 90; n = 38 events; 22 cells with at least one applicable event; $p = .567$) and the dwell time was 0.13 s (Q1, 0.05; Q3, 0.61; n = 116 events; 30 cells with at least one applicable event) versus 0.12 s (Q1, 0.05; Q3, 0.54; n = 85 events; 40 cells with at least one applicable event; $p = .960$) for NB+ and DMEM+ astrocytes, respectively (Figure S4b,c).

At rest, vesicles that interacted with the plasmalemma exhibit similar amplitude (size) and frequency in astrocytes from both cultures (Figure 2b,c; Table S1). However, in NB+ astrocytes, increased G_p and prolonged dwell time were recorded in reversible exocytosis (Figure S4). Because both parameters depend on $[Ca^{2+}]_i$ (Gucek et al., 2016), it is possible that NB+ astrocytes exhibit different Ca^{2+} signaling patterns. Therefore, we stimulated DMEM+ and NB+ astrocytes with 100 μM ATP to increase $[Ca^{2+}]_i$ (Figure S5). In DMEM+ astrocytes (n = 31 cells), this stimulation increased the frequency of both full and reversible exocytosis: 0.15 ± 0.03 events/min versus 0.27 ± 0.05 events/min ($p = .010$) and 0.47 ± 0.07 events/min versus 0.66 ± 0.09 events/min ($p = .011$), respectively, as well as reversible endocytosis: 0.20 ± 0.05 events/min versus 0.51 ± 0.19 events/min ($p = .031$). Moreover, a robust decrease in the frequency of full endocytosis was detected upon ATP stimulation: 1.07 ± 0.14 events/min versus 0.48 ± 0.07 events/min ($p < .001$) (Figure S5a). ATP stimulation attenuated the frequency of full endocytosis in NB+ astrocytes (n = 26 cells): 1.03 ± 0.16 events/min versus 0.55 ± 0.09 events/min ($p = .005$). Conversely, the frequency of other exo−/endocytotic event types remained unaltered: 0.21 ± 0.05 events/min versus 0.36 ± 0.11 events/min ($p = .258$) and 0.44 ± 0.12 events/min versus 0.93

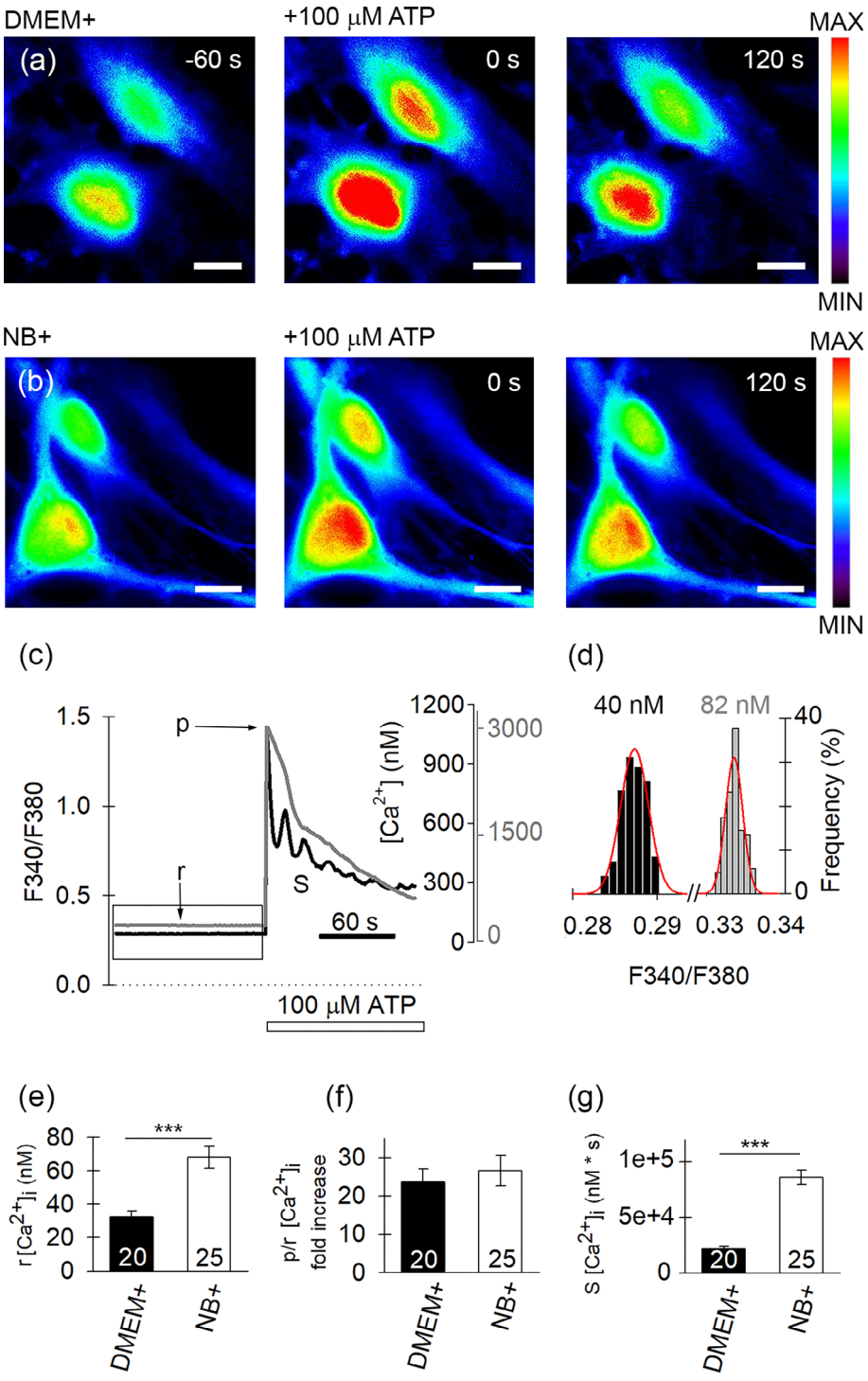

FIGURE 3 Resting and ATP-evoked increase in $[Ca^{2+}]_i$ differ in DMEM+ and NB+ astrocytes. (a), (b) Epifluorescent images of serum ((a), DMEM+) and arborized ((b), NB+) astrocytes loaded with the Ca^{2+} indicator Fura-2, before (−60 s) and during (0 and 120 s) ATP stimulation (100 μM), which increased $[Ca^{2+}]_i$. the increase in $[Ca^{2+}]_i$ is depicted on a pseudocolor scale (right: Minimum F340, black; maximum F340, red). Scale bars, 20 μm. (c) Examples of time-dependent Fura-2 emission ratio (F340/F380 left) and $[Ca^{2+}]_i$ (nM, right) measured in DMEM+ (black trace) and NB+ (gray trace) astrocytes after stimulation with ATP (100 μM); b denotes baseline $[Ca^{2+}]_i$, p denotes peak $[Ca^{2+}]_i$, and S is the area under the curve. The increase in F340/F380 ratio evoked by ATP (white horizontal bar) indicates an increase in $[Ca^{2+}]_i$ (ordinates on the right of the plots; black, DMEM+; gray, NB+ astrocytes, taking into account respective Fura-2 calibration curves for each culture). (d) The relative frequency distribution (in %) of ratio values (F340/F380) obtained during the 120 s resting period (indicated by box in (c)). These data were fitted with the Gaussian function $f = a \times \exp(-0.5 \times ([x - x_0]/b)^2)$, where $a = 30.60 \pm 2.08$, $b = 0.00 \pm 0.00^{-0.5}$, $x_0 = 0.29 \pm 0.00$ (black frequency plot) in DMEM+ astrocytes and $a = 32.18 \pm 4.75$, $b = 0.00 \pm 0.00^{-0.5}$, $x_0 = 0.33 \pm 0.00$ (gray frequency plot) in NB+ astrocytes. The parameter x_0 is used here to represent the baseline $[Ca^{2+}]_i$ (displayed in nM; baseline $[Ca^{2+}]_i$ values were calculated from the DMEM+ and NB+ calibration curves) in both astrocyte cultures. Note the higher baseline $[Ca^{2+}]_i$ in NB+ astrocytes. (e) Baseline $[Ca^{2+}]_i$; ***$p < .001$ (Mann–Whitney *U*-test). (f) Peak over baseline fold increase in $[Ca^{2+}]_i$. (g) Area under the curve measured for 120 s ATP stimulation; ***$p < .001$ (Mann–Whitney *U*-test). Data displayed in (e), (f), and (g) (mean ± SEM) were obtained in 20 DMEM+ and 25 NB+ astrocytes

± 0.26 events/min ($p = .061$), for full and reversible exocytosis, respectively, and 0.34 ± 0.11 events/min versus 0.35 ± 0.14 events/min ($p = .927$) for reversible endocytosis (Figure S5b). The Wilcoxon signed-rank test was used to statistically evaluate differences in exo−/endocytotic frequencies in astrocytes before and after ATP stimulation. Collectively, our data indicate that ATP-evoked modulation of single-vesicle exo−/endocytosis is less pronounced in NB+ compared with DMEM+ astrocytes.

3.4 | NB+ astrocytes exhibit distinct resting and ATP-evoked changes in $[Ca^{2+}]_i$

Differences in vesicle mobility (Figure 1; Figure S3) and exo−/endocytotic activity (Figures S4 and S5) may reflect distinct Ca^{2+} homeostasis in DMEM+ and NB+ astrocytes. Therefore, we next measured resting and ATP-evoked increases in $[Ca^{2+}]_i$ by microfluorimetry in DMEM+ and NB+ astrocytes loaded with the fluorescent Ca^{2+}

indicator Fura-2 and imaged individual cells before and after ATP application (Figure 3a,b).

At rest, the mean baseline $[Ca^{2+}]_i$ was ~2-fold higher in NB+ versus DMEM+ astrocytes: 68 ± 6 nM (n = 25 cells) versus 33 ± 3 nM (n = 20 cells); $p < .001$; Mann–Whitney *U*-test (Figure 3c–e), respectively. We also examined spontaneous changes in $[Ca^{2+}]_i$, localized to subcellular microdomains, in astrocytes loaded with Fluo-4 AM (Figure S6a–d). The frequency of microdomain Ca^{2+} spikes was higher in NB + astrocytes, 0.45 ± 0.02/min (n = 280 microdomains, n = 32 cells) versus DMEM+ astrocytes, 0.30 ± 0.02/min (n = 61 microdomains, n = 30 cells; $p < .05$; Figure 4e), whereas relative peak $[Ca^{2+}]_i$ amplitude and the amount of mobilized $[Ca^{2+}]_i$ during Ca^{2+} spikes did not differ in astrocytes from both cultures (Figure S6f,g), as reported previously (Wolfes et al., 2017).

Next, we examined ATP-evoked $[Ca^{2+}]_i$ responses in Fura-2-loaded DMEM+ (Figure 3a) and NB+ (Figure 3b) astrocytes. After application of 100 μM ATP, the average peak-to-baseline (p/b) ratio of the $[Ca^{2+}]_i$ increase was similar in NB+ and DMEM+ cells; 22-fold and 25-fold, respectively (Figure 3f). However, the area under the curve (S), estimated for the first 120 s after ATP stimulation, was 3-fold higher in NB+ astrocytes than in DMEM+ astrocytes ($p < .001$; Mann–Whitney *U*-test; Figure 3g), likely due to distinct kinetics of $[Ca^{2+}]_i$ responses. Indeed, three types of ATP-evoked $[Ca^{2+}]_i$ responses were observed in astrocytes from both cultures: transient, sustained, and oscillatory (Figure S7a,b). The fraction of cells with the transient responses was similar in DMEM+ and NB+ astrocytes, about a quarter of total cell population (Table S2). However, the percentage of sustained and oscillatory responses differed in DMEM+ and NB+ cells. In DMEM+ cells, the oscillatory responses were predominant (72%) as confirmed by continuous wavelet transform analysis (see Section 2 and Figure S7c), whereas in NB+ cells, sustained responses prevailed (72%). The most characteristic oscillation periods fall in the range between 11 and 20 s in DMEM+ astrocytes (55% of the total cell population; Figure S7d). Only 4% of NB+ astrocytes displayed oscillatory responses with a discernible oscillation period in the range between 21 and 30 s. In summary, NB+ astrocytes display higher resting $[Ca^{2+}]_i$, higher frequency of spontaneous Ca^{2+} spikes, and diminished frequency of ATP-evoked oscillatory $[Ca^{2+}]_i$ responses in comparison with DMEM + astrocytes.

To further validate findings of stimulus-evoked Ca^{2+} signaling in rat astrocyte cultures, we next examined NA-evoked Ca^{2+} signaling in SR 101-labeled astrocytes in acute rat brain slices (Nimmerjahn et al. 2004) and to our knowledge, for the first time, also in primary cultured human DMEM+ astrocytes. Application of NA (10 μM) evoked an increases in $[Ca^{2+}]_i$ with a similar peak (relative-to-baseline (p/b)) amplitude in all astrocytes examined; in cultured rat DMEM+ and NB+ astrocytes, in cultured human DMEM+ astrocytes, and in acute rat brain slice astrocytes (Figure S8). With the exceptions of rat NB+ and hDMEM+ astrocytes, in which the average peak NA-evoked increases in $[Ca^{2+}]_i$ were larger when compared to rat DMEM+ astrocytes. However, the peak responses in $[Ca^{2+}]_i$ were similar (Figure S8).

3.5 | Subcellular $[cAMP]_i$ heterogeneity is similar in DMEM+ and NB+ astrocytes

Signaling mediated with cAMP is pivotal for the regulation of astrocyte morphology (Horvat & Vardjan, 2019; Koyama et al., 1993; Vardjan et al., 2014; Won & Oh, 2000), and it may differ between DMEM+ and NB+ astrocytes. To examine whether cAMP production differs in astrocytes from different cultures, astrocytes were non-enzymatically detached from multiwell plates and exposed to the amplified luminescent proximity homogenous assay (ALPHA, see Materials and methods). The cAMP calibration curve was used to convert the measured ALPHA signals to the quantity of cAMP molecules produced in a suspension of astrocytes from a given culture (EC_{50} of 6.21 ± 0.42 nM; Figure S9a). The capacity of cAMP production, determined as the cAMP molecules released per unit time from cell lysates (12 independent measurements, each in triplicate, prepared from two cultures), revealed a similar production rate in both cultures (Figure S9b).

To study cAMP homeostasis at the cellular level, DMEM+ and NB+ astrocytes were transfected with FRET-based cAMP nanosensor Epac1-camps (Figure 4a,b), which reports $[cAMP]_i$ with EC_{50} ~ 1 μM (Borner et al., 2011). At rest, the nanosensor CFP/YFP ratio was relatively homogeneously distributed inside individual cells from both cultures (Figure 4c,d). However, the average resting CFP/YFP ratio appeared higher in NB+ astrocytes than in DMEM+ astrocytes, indicating increased resting $[cAMP]_i$ in NB+ astrocytes (Figure 4f,g). Although ratiometric fluorescence measurements are conceptually devoid of artifacts associated with heterogeneous subcellular distribution of the nanosensor within the cell (Grynkiewicz et al., 1985), we analytically examined this possibility as well. We thus calculated the Pearson correlation coefficient (R) between the normalized sum of CFP and YFP fluorescence intensity (CFP + YFP), reporting the amount of fluorophore in a given cell region, and the normalized fluorescence ratio (CFP/YFP), a measure of $[cAMP]_i$, on a pixel-by-pixel basis (in total 491,133 Epac1-camps-positive pixels) from 8 images of DMEM+ astrocytes (Figure S10a–t). The calculated R was 0.05 (Figure S10t), indicating that region-specific differences in the local amount of nanosensor are unlikely to affect the ratiometric estimate of $[cAMP]_i$.

As the resting $[cAMP]_i$ appeared higher in NB+ astrocytes than in DMEM+ astrocytes (0.62 ± 0.01 μM versus 0.57 ± 0.01 μM; $p < .01$; Figure 4g) we next examined whether NA-evoked changes in $[cAMP]_i$ also differ in astrocytes from both cultures. The application of 100 μM NA evoked a time-dependent exponential increase in the CFP/YFP ratio (Figure 4e). The maximum amplitude and the time constant of the NA-evoked increase in $[cAMP]_i$ were similar in both cultures (Figure 4h,i), suggesting that noradrenergic, G-protein coupled receptor mediated cAMP signaling, on a global cell scale, is operating similarly in DMEM+ and NB+ astrocytes.

Further, to learn whether subcellular, microdomain-like, heterogeneity exists in resting and/or NA-evoked changes in $[cAMP]_i$, we analyzed small ROIs positioned along a line in the perpendicular direction from the cell nucleus toward the periphery/processes (Figure 5a,b,e,f).

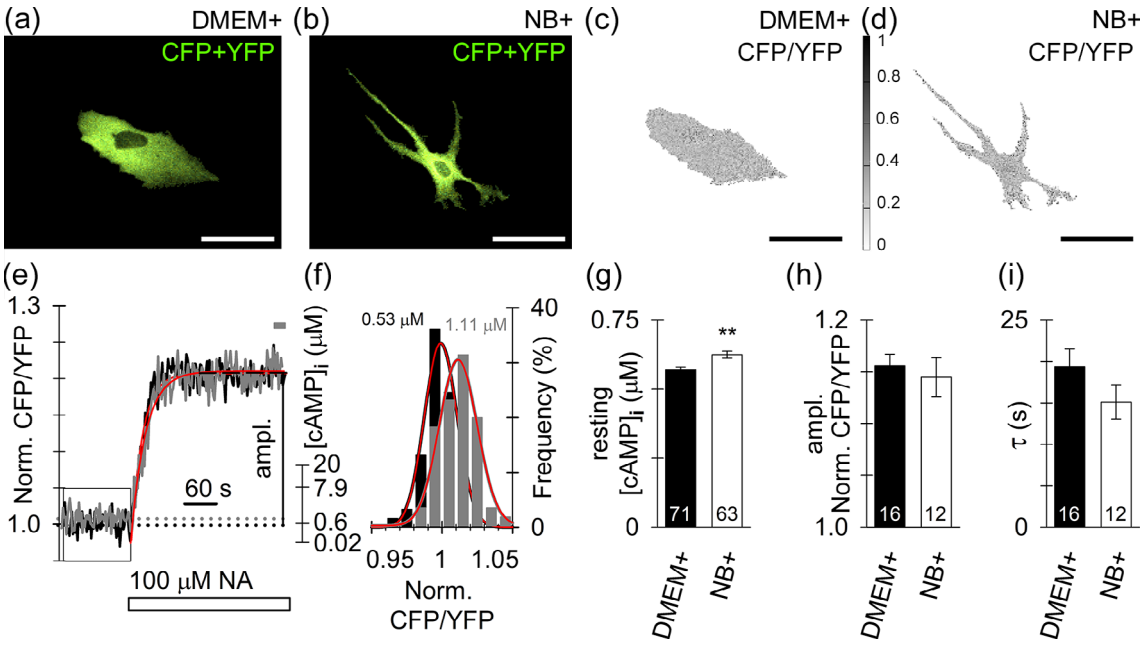

FIGURE 4 Resting $[cAMP]_i$ is higher in NB+ astrocytes, whereas noradrenaline (NA) evokes a similar increase in $[cAMP]_i$ in astrocytes from both cultures. (a,b) confocal micrographs display resting DMEM+ (a) and NB+ (b) astrocytes, expressing the cAMP nanosensor Epac1-camps (merged CFP and YFP emissions visible as yellow-green fluorescence; note the apparent spatial inhomogeneity of the fluorescence intensity signal). (c,d) inverted grayscale micrographs (images shown in (a) and (b)) display ratio images calculated by division of CFP with YFP fluorescence intensity (CFP/YFP) with the lowest ratio value in white (0) and the highest value in black (1). Scale bars, 50 μm (a–d). Note that ratio images (c,d) display a spatially homogeneous fluorescence ratio signal indicative of a homogeneous subcellular distribution of $[cAMP]_i$ in resting DMEM+ and NB+ astrocytes. (e) Time-dependent changes of the Epac1-camps emission ratio (CFP/YFP, left) and $[cAMP]_i$ (μM, right) measured in DMEM+ (black trace) and NB+ (gray trace) astrocytes after stimulation with NA (100 μM). The monophasic increase in FRET signal (CFP/YFP) evoked by NA (white rectangle) indicates an increase in $[cAMP]_i$ (ordinate on the right of the plots). Single-exponential increase to maximum function (red; $f = y_0 + a \times (1 - \exp[-b \times x])$, where $\tau = 1/b$; see Materials and methods) was fitted to the time-dependent changes in the normalized ratio CFP/YFP. (f) The relative frequency distribution (in %) of normalized ratio values (CFP/YFP) obtained during a 120 s resting period (indicated by box in e). These data were fitted with the Gaussian function $f = a \times \exp(-0.5 \times ([x - x_0]/b)^2)$, where $a = 33.49 \pm 2.87$, $b = 0.01 \pm 0.00^{-0.5}$, $x_0 = 0.99 \pm 0.00$ (black frequency plot) in DMEM+ and $a = 30.29 \pm 2.25$, $b = 0.01 \pm 0.00^{-0.5}$, $x_0 = 1.01 \pm 0.00$ (gray frequency plot) in NB+ astrocyte, respectively. The parameter x_0 was used to calculate the baseline $[cAMP]_i$ (displayed in μM [Lasič et al., 2019]) in both astrocyte cultures. Note the higher baseline $[cAMP]_i$ in NB+ astrocytes. (g) Averaged resting cytosolic level of cAMP (in μM, see material and methods for calibration) is increased in NB+ astrocytes compared with DMEM+ astrocytes. $^{**}p < .01$ (Mann–Whitney *U*-test). (h), (i) the maximum amplitude of NA-evoked increase in normalized CFP/YFP (averaged over the last 20 s of stimulation indicated by the gray label in (e)) (h) and the time constant (τ) of the increase (i) in DMEM+ and NB+ astrocytes. Numbers at the bottom of the bars indicate the number of nonstimulated (g) or NA-stimulated (h,i) cells analyzed

We examined time-dependent changes in the CFP/YFP ratio before and after NA stimulation (100 μM; Figure 5c,d,g,h). In a single small ROI, we recorded a NA-induced monophasic increase in the CFP/YFP ratio (microdomain, Figure 5c,g), which shared similarity with the time-dependence of the CFP/YFP ratio obtained in the entire cell (Figure 4e). Generally, the average ROI signal of individual microdomains was noisier than the signal obtained from the whole cell soma, likely due to a relatively small number of image pixels constituting the small ROI. By plotting all averaged CFP/YFP ratios (normalized to 0–1) from all ROIs sampled along a given line, we constructed kymographs and observed a relatively uniform time-dependent increase in $[cAMP]_i$. Two kymographs are displayed in Figure 5d,h, where the abscissa represents time and the ordinate is the distance from the nucleus (as successive ROI numbers), and the normalized CFP/YFP ratio at a given cell position is pseudocolor-coded (warm colors represent a relatively higher value of the CFP/YFP ratio). In astrocytes from both cultures, the intensity of the CFP/YFP signal increased with the distance from the nucleus; in soma as well as in the processes (Figure 5d,h).

Moreover, when analyzing changes in the microdomain CFP/YFP ratio along each of the separate directions in DMEM+ and NB+ astrocytes, at rest and after NA stimulation, we observed three types of subcellular heterogeneity in $[cAMP]_i$ (Figure 6). In resting (Figure 6a) and NA-stimulated (Figure 6b) conditions, we recorded an increase, a decrease, or no change in $[cAMP]_i$ along the perpendicular direction from the nucleus to the periphery. Table S3 lists the slope coefficients of lines representing gradients in $[cAMP]_i$, and corresponding statistical significances; a summary of the numbers of cells analyzed, linear paths, and the number of ROIs analyzed is listed in Table S4. When analyzing changes in the regional CFP/YFP ratio over the distance in resting cells, we mostly did not observe significant change in either DMEM+ (18/22 paths) or NB+ (13/20 paths)

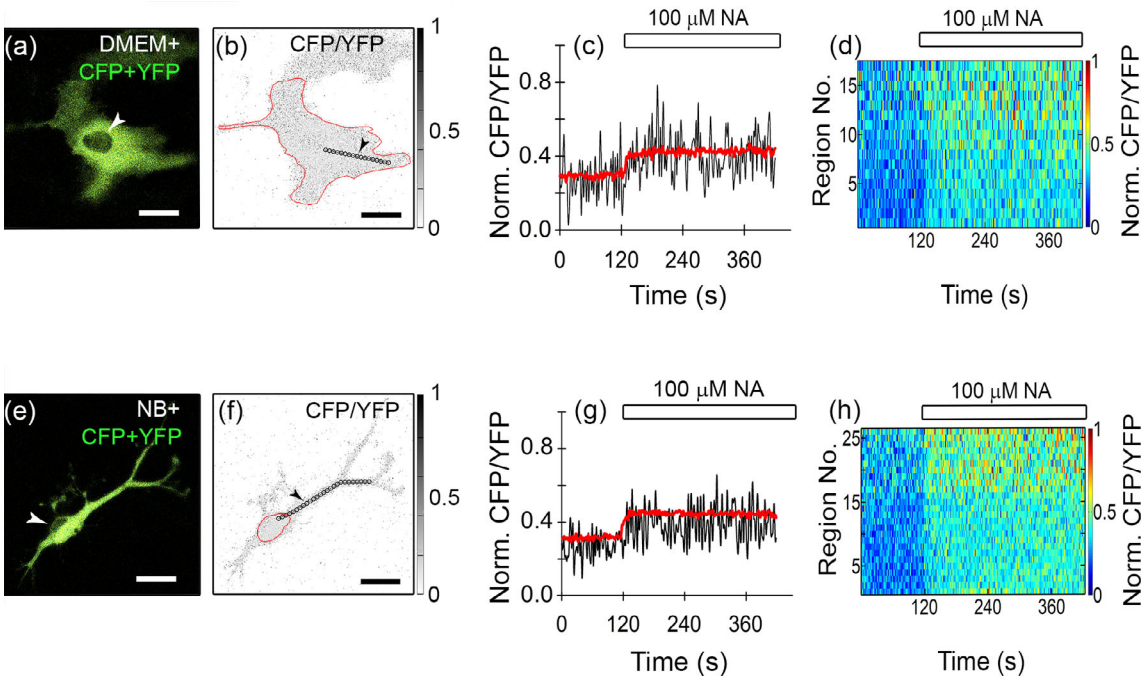

FIGURE 5 Subcellular heterogeneity (microdomain analysis) of time-dependent NA-evoked increase in $[cAMP]_i$ in the direction from the cell nucleus toward the periphery. (a), (e) Merged CFP and YFP emission images of DMEM+ (a) and NB+ (e) astrocytes; white arrowheads point to the cell nuclei. (b), (f) Inverted grayscale CFP/YFP ratio images of DMEM+ (b) and NB+ (f) astrocytes with the lowest ratio values in white (0) and highest ratio values in black (1). Cell soma is outlined (red line). Black circles (diameter 2 μm) indicate regions of interest (ROIs) placed along a line drawn in the perpendicular direction from the cell nucleus toward the periphery/processes. Black arrowheads point to a certain ROI in a given set of analyzed ROIs. Scale bars (a), (b), (e), (f), 20 μm. (c), (g) Averaged, time-dependent increases in $[cAMP]_i$ in the whole cell (or soma, red line) and in the ROI indicated by the arrowhead (see b and f; black line; ~18 μm from the cell nucleus) where the CFP/YFP ratio signal was normalized to 0–1 per cell encompassing all ROIs in that cell across all time points (1 denotes the highest CFP/YFP ratio value across all analyzed ROIs and time points in each single cell, whereas 0 denotes the lowest CFP/YFP ratio value obtained; see Materials and methods for the formula used), evoked by 100 μM NA (white rectangle) in DMEM+ (c) and NB+ (g) astrocytes. (d), (h) Time-resolved pseudocolored kymograph image of NA-evoked increase in $[cAMP]_i$ (CFP/YFP ratio, normalized to 0–1 per cell) measured in all ROIs positioned in sequence along a single line drawn in the perpendicular direction from the cell nucleus toward the periphery/processes (obtained from images (b,f); the region closest to the cell nucleus is displayed at the bottom, and the most distant region is displayed at the top of the kymograph chart y-axis. Note that application of NA (white rectangle, 100 μM) evoked a synchronous increase in the CFP/YFP ratio in all ROIs positioned along the given line in astrocytes. Notably, the CFP/YFP ratio (indicated by warm colors) apparently increased in the direction from the cell nucleus toward the periphery. Circular ROIs displayed in the images (b) and (f) are examples of directions along which the CFP/YFP ratio increased with the distance from the nucleus. The increase in the CFP/YFP ratio is depicted on a pseudocolor scale ((d) and (h), right), normalized to 0–1 with dark blue representing the lowest and red the highest ratio value

astrocytes. Representative paths are displayed in Figure 6aa and ad, respectively. In addition, we found cases of either a statistically significant positive trend (DMEM+, 3/22 paths; NB+, 3/20 paths) or a negative trend in subcellular $[cAMP]_i$ distribution (DMEM+, 1/22 paths; NB+, 4/20 paths). If a significant positive or negative trend along a particular direction was observed in the resting state, either in DMEM + or NB+ cells (Figure 6ab, ac, ae, af, respectively), it was also observed after stimulation in the same cell (Figure 6 bb, bc, be, bf, respectively). This indicates a putative interdependence between the levels in $[cAMP]_i$ before and after stimulation with NA. Next, we pooled the data for the normalized resting CFP/YFP ratio from many ROIs and plotted them versus the data for the normalized stimulated CFP/YFP ratio; separately for DMEM+ (no. of ROIs, 219) and NB+ cells (no. of ROIs, 250) (Figure 6c). In astrocytes from both cultures, we found a significantly positive correlation ($R_{DMEM+} = 0.66$ and $R_{NB+} = 0.84$). Slopes of linear regression lines fitted to data differed significantly one from another ($p < .001$). These data indicate that microdomains with lower resting $[cAMP]_i$ will reach relatively lower $[cAMP]_i$ levels upon stimulation with NA, and that subcellular microdomains with relatively higher resting $[cAMP]_i$ will attain relatively higher $[cAMP]_i$ levels upon NA stimulation. In addition, we examined whether the intensity of the regional response to NA stimulation changes with respect to the distance from the nucleus. For this, we pooled data from ROIs, separately for DMEM+ and NB+ cells, and subtracted the resting CFP/YFP ratio from the stimulated CFP/YFP ratio (a measure of the localized change in $[cAMP]_i$). We plotted this difference versus the distance from the nucleus and fitted the data with the linear regression function of the form $y = k \times x + n$, where y represents the difference between the stimulated CFP/YFP ratio and the resting CFP/YFP ratio; x is the distance from nucleus (μm); k

represents the slope of the regression line (μm^{-1}) and n is the y intercept. Linear functions revealed a relatively small, but significant trend for cAMP production in astrocytes from both cultures, which also differed one from another ($p < .01$; Figure 6d). DMEM+ cells exhibited a negative trend ($p < .05$), possibly suggesting slightly diminished capacity for NA-evoked cAMP production in regions closer to the cell periphery (Figure 6d, left). In contrast, NB+ cells displayed a positive trend ($p < .001$), suggesting a slightly enhanced cAMP production in response to NA stimulation in the cell processes (Figure 6d, right).

4 | DISCUSSION

Previous studies on cultured astrocytes revealed that Ca^{2+} signaling is phasic and fast, whereas cAMP signaling exhibits tonic and slower

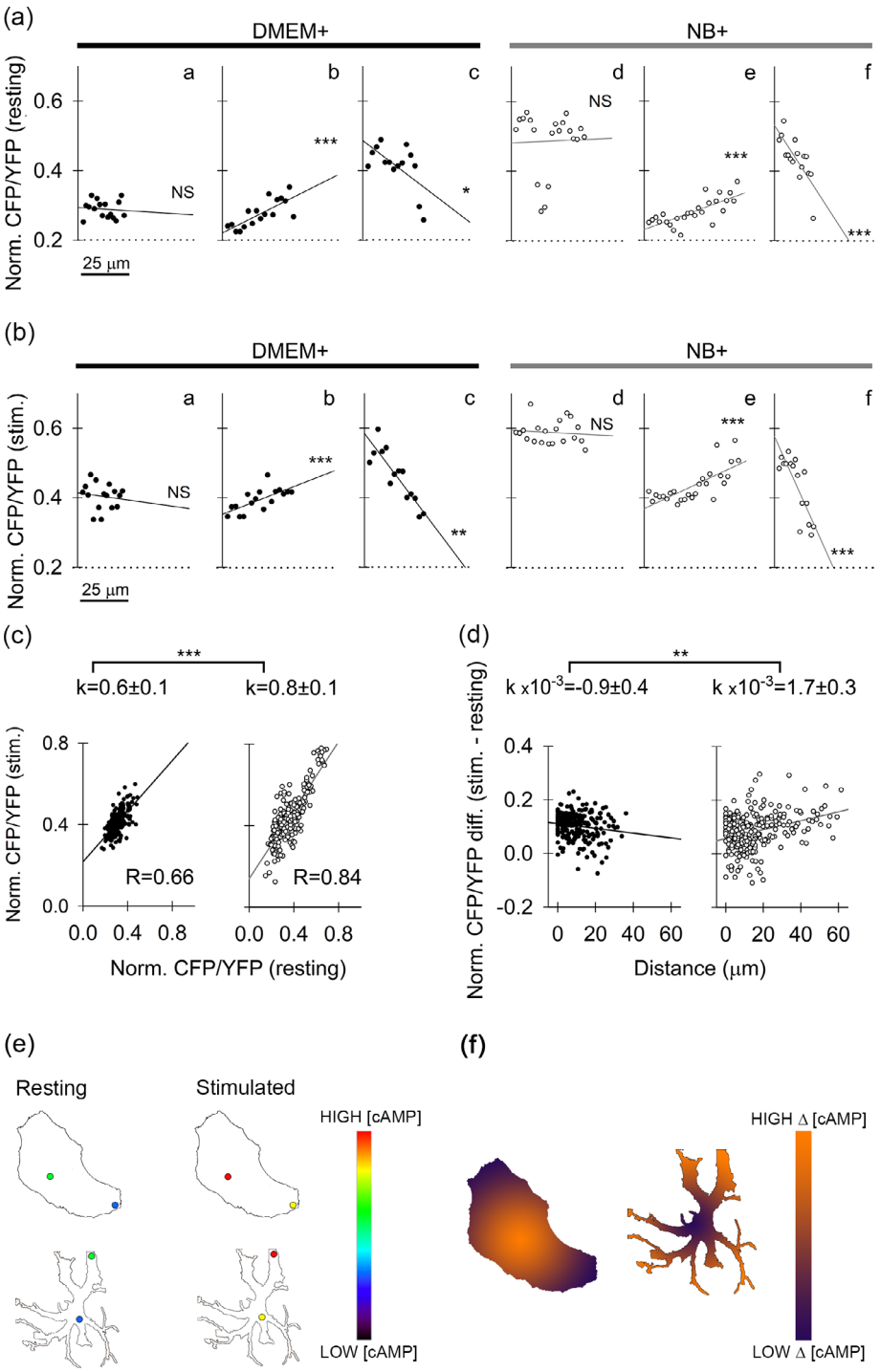

FIGURE 6 Legend on next page.

dynamics (Horvat et al., 2016), which was subsequently confirmed in an in vivo system (Oe et al., 2020), validating the use of cultured cells to study basic cell processes. Here, we compared the functional plasticity and Ca^{2+} and cAMP signaling of astroglia grown in serum-free media promoting process-bearing arborization (NB+) (Wolfes et al., 2017; Wolfes & Dean, 2018), and in the presence of serum (DMEM+), a condition similar for pathology-related reactive astrocytes with a compromised blood/brain barrier (Foo et al., 2011; Zamanian et al., 2012). The main findings revealed functional changes imposed by the two dissimilar culture conditions, each providing an insight into the plasticity that astrocytes may encounter in vivo. The NB+ astrocytes displayed attenuated vesicle traffic and altered vesicle interaction with the plasma membrane. Emergence of process-bearing phenotypes was associated with increased resting levels in $[cAMP]_i$, and enhanced subcellular heterogeneity in $[Ca^{2+}]_i$, but subcellular heterogeneity in the NA-evoked increase in $[cAMP]_i$ was unaffected by the culture environment promoting arborization.

4.1 | Fewer NB+ astrocytes express nestin and GFAP

Nestin is expressed in proliferating progenitor cells (Bernal & Arranz, 2018; Messam et al., 2000). Although the proportion of nestin-positive cells was high in both cultures, confirming previous report (Wolfes et al., 2017), we found that a significantly lower proportion of NB+ astrocytes expressed nestin (Figure S1c,d), suggesting that these cells exhibit a different status as DMEM+ astrocytes. In addition to GFAP, a commonly used marker for astrocytes, we tested the presence of MFGE8, a marker for telencephalon astrocytes (Zeisel et al., 2018). We asked whether the expression of these proteins can also be utilized to discriminate subtypes of astrocytes in both cultures. Whereas MFGE8 was ubiquitously expressed, the proportion of GFAP-expressing cells was lower in NB+ astrocytes versus DMEM+ astrocytes (Figure S2). As the GFAP expression may indicate increased astrocyte reactivity (Sofroniew, 2009; Yang & Wang, 2015), NB+ astrocytes are potentially less reactive. An alternative explanation for less abundant GFAP expression in NB+ astrocytes is tied to hbEGF, which at concentrations >10 ng/ml, causes de-differentiation of astrocytes (Puschmann et al., 2014).

4.2 | Decreased vesicle mobility in NB+ astrocytes is associated with increased resting $[Ca^{2+}]_i$

Our results revealed that spontaneous mobility of vesicles in NB+ astrocytes is reduced in comparison with DMEM+ astrocytes (Figure 1). Astroglial $[Ca^{2+}]_i$ affects vesicle mobility (Potokar et al., 2013), therefore it is likely that altered vesicle mobility is due to differences in resting $[Ca^{2+}]_i$ in NB+ versus DMEM+ astrocytes (Figure 3). In addition, vesicle traffic is associated with the cytoskeleton (Potokar et al., 2007), and differences in vesicle mobility may be due to different cytoskeletal fabrics in DMEM+ astrocytes, which produce stress fibers that contain bipolar arrays of actin and myosin type II (John et al., 2004). NB+ astrocytes lack stress fibers and possess Arp2/3-dependent actin networks (Murk et al., 2013). Moreover, RhoA GTPase, involved in stress fiber formation, is inactive in NB+ astrocytes (O'Shea et al., 2015; Racchetti et al., 2012). As RhoA GTPase activity is linked to a decreased expression of genes encoding molecular motors (O'Shea et al., 2015), this may additionally inhibit vesicle mobility in NB+ astrocytes.

While vesicle mobility was altered in both types of astrocytes, membrane capacitance measurements revealed similar exo−/endocytotic activity in DMEM+ and NB+ astrocytes (Figure 2), with the sole

FIGURE 6 Subcellular $[cAMP]_i$ heterogeneity in DMEM+ and NB+ astrocytes. (a), (b) Representative examples of distance-dependent resting (a) and NA-evoked (stimulated) (b) changes in $[cAMP]_i$ (CFP/YFP ratio, normalized to 0–1, encompassing all ROIs per cell and averaged for 30 s at the beginning and at the end of the signal recording to estimate resting and stimulated $[cAMP]_i$; see Materials and methods) in DMEM+ astrocytes (aa), (ab), (ac), (Ba), (bb), (bc); black circles and regression lines) and NB+ astrocytes (ad), (ae), (af), (bd), (be), (bf); white circles, gray regression lines) along selected directions from the cell nucleus toward the cell periphery/processes. All types of changes that were observed in DMEM+ as well as NB+ cells are displayed: Directions along which $[cAMP]_i$ did not change with distance from cell nucleus (aa, ad, ba, bd), directions along which $[cAMP]_i$ significantly increased with distance from the nucleus (ab, ae, bb, be) and directions along which $[cAMP]_i$ significantly decreased with distance from the nucleus (ac, af, bc, bf). Typically, a significantly positive or negative trend observed in resting conditions was also mirrored after cell stimulation (ab)-(bb), (ac)-(bc), (ae)-(be), (af)-(bf). (c) Graphs displaying normalized resting values plotted versus normalized NA-stimulated values reveal a high degree of correlation, especially in NB+ cells ($R = 0.84$). This means that cells with higher resting $[cAMP]_i$ will likely end up with a relatively higher $[cAMP]_i$ after NA stimulation. Both DMEM+ (black circles, black regression line) and NB+ (white circles, gray regression line) slopes were significantly positive ($p < .001$, Student's *t*-test), and significantly different from each other ($p < .001$, Student's *t*-test). (d) Relationship between the difference in normalized values of stimulated-resting CFP/YFP ratio and the distance from the nucleus. DMEM+ cells (black circles, black regression line) display a statistically significant negative trend with a low negative slope coefficient, meaning that capacity for NA-stimulated cAMP production weakens in the direction from the cell nucleus toward the periphery. In contrast, NA-stimulated cAMP production in NB+ cells increases in the direction from the cell nucleus (white circles, gray regression line), and the regression line displays a positive slope. (e) Simplified drawings of a DMEM+ (top) and NB+ astrocyte (bottom) in resting and stimulated states with two circular regions symbolically depicting microdomains where cAMP concentration was measured (to obtain data represented in panel c). Cold colors in the pseudo-color intensity scale indicate regions with lower, whereas warmer colors indicate regions with higher [cAMP], respectively. (f) Simplified drawings of a DMEM+ (left) and NB+ astrocyte (right) depicting region-dependent difference (Δ) between stimulated and resting [cAMP] microdomain data represented in panel d. Low difference between the stimulated and the resting [cAMP] is displayed by violet, whereas high difference by an orange color on the pseudo-color intensity scale

exception of a modulatory effect on the fusion pore properties in vesicles undergoing reversible exocytosis (Figure S4), a finding consistent with the increased resting level of cAMP in NB+ astrocytes (Figure 4, see also [Lasič et al., 2019]). This may reflect differential expression of vesicle-associated proteins involved in exo−/endocytosis in NB+ versus DMEM+ astrocytes (Wolfes et al., 2017). The exo−/endocytotic response to ATP-evoked increase in $[Ca^{2+}]_i$ was less pronounced in NB+ astrocytes (Figure S5). In NB+ astrocytes, the reduced vesicle ability to enter into Ca^{2+}-evoked exocytosis (Figure 2) could be explained by higher basal $[Ca^{2+}]_i$ (Figure 3), shown previously to attenuate secretory vesicles delivery to the plasma membrane (Stenovec et al., 2016). Moreover, this may be due to a combination of altered dynamics of ATP-evoked $[Ca^{2+}]_i$ responses (Figure S7), preferential segregation of VAMP2 vesicles to thin processes of arborized astrocytes (Wolfes et al., 2017) and/or differential expression of vesicle-associated proteins regulating Ca^{2+}-dependent exo−/endocytosis (Vardjan & Zorec, 2015). In astrocyte cultures several isoforms (Syt; Syt4, 7, 11 & 17) of synaptotagmins putatively involved in modulating Ca^{2+}-regulated exocytosis (Sudhof, 2012; Zhang et al., 2009) were identified (Wolfes et al., 2017)). None of the Syt isoforms co-localized with VAMP2 vesicles in NB+ astrocytes (Wolfes et al., 2017). This finding contrasts an earlier report, in which Syt4 was found on immunoisolated VAMP2 vesicles from cultured hippocampal DMEM+ astrocytes (Crippa et al., 2006). Syt4 also co-localized with secretory peptidergic vesicles (Stenovec et al., 2016) and recycling vesicles in cultured cortical DMEM+ astrocytes (Lasic et al., 2017; Potokar et al., 2008). These disparities are noteworthy, since Syt4 was proposed to regulate astroglial exocytosis (Zhang et al., 2004). The discrepancy in Syt4 co-localization with VAMP2 vesicles in astrocytes from both cultures could partially explain diminished ATP-evoked exocytosis and modulation of narrow fusion pore properties during reversible exocytosis in NB+ astrocytes. Moreover, the expression of various Syt isoforms in astrocytes can be further modulated by second messengers, including cAMP (Paco et al., 2016), the resting level of which was found increased in NB+ astrocytes (Figure 4).

4.3 | NB+ astrocytes exhibit different $[Ca^{2+}]_i$ dynamics than DMEM+ astrocytes

Our results revealed increased resting $[Ca^{2+}]_i$ in NB+ astrocytes compared with DMEM+ astrocytes (68 nM versus 33 nM; Figure 3) and identified three basic types of ATP-evoked $[Ca^{2+}]_i$ responses: transient, sustained, and oscillatory (Yoshida et al., 2005). The predominant type of Ca^{2+} response (Table S2, see also Figure S7) was sustained in NB+ astrocytes and oscillatory in DMEM+ astrocytes. Besides ATP, histamine, glutamate, and noradrenaline (Morita et al., 2003; Morita et al. 2015a; Pasti et al., 1995) trigger $[Ca^{2+}]_i$ oscillations in astrocytes and other cells (Morita et al., 2003; Morita, Nakane, Fujii, et al., 2015; Piazza et al., 2007). The majority (77%) of oscillatory responses in DMEM+ astrocytes had a characteristic oscillation period of 11–20 s, which is in agreement with the oscillation period reported for responses evoked by NA or glutamate (Horvat et al., 2016; Morita et al., 2003; Pasti et al., 1995). At its core, the oscillatory pattern is governed by the rate of Ca^{2+} influx mediated by Ca^{2+}-induced Ca^{2+} release through InsP3 receptors (De Pitta et al., 2009). Notably, the majority of NB+ astrocytes responded with a sustained increase in $[Ca^{2+}]_i$ (Table S2), possibly due to Ca^{2+} influx through $P2X_7$ purinoceptors ($P2X_7R$) (Nobile et al., 2003). Predominantly sustained (in NB+ astrocytes) or oscillatory (in DMEM+ astrocytes) responses may arise from different ratios of surface P2YRs and P2XRs due to different gene expression in both cultures (Wolfes et al., 2017). DMEM+ astrocytes potentially express more P2YRs, whereas NB+ astrocytes express more P2XRs. Alternatively, different responses may arise from the adenosine receptors that affect $[cAMP]_i$ (Alloisio et al., 2004). Calcium oscillations were linked to the activity of protein kinase C (Nash et al., 2002) and its modulatory effect (Bartlett et al., 2015; Morita et al. 2015b) via increased SERCA expression that upregulated Ca^{2+} oscillations (Morita & Kudo, 2010). A recent article (Mikolajewicz et al., 2021) also describes a complex interplay between receptors in cells exposed to increasing ATP concentration, resulting in shift between transient and oscillatory type of $[Ca^{2+}]_i$ responses. At 100 μM ATP appears to elicit oscillatory, transient and sustained responses (Figure S7). Among many factors, including interactions between Ca^{2+} and cAMP signaling, these responses may be determined by relative expression levels (active number) of either metabotropic or ionotropic receptors; the most likely explanation regarding why NB+ astrocytes exhibit more sustained Ca^{2+} responses and less oscillatory. HB-EGF application was shown to increases the number of oscillations in astrocytes stimulated by aminocyclopentane-1,3-dicarboxylic acid (ACPD) or glutamate (Morita et al., 2003; Morita et al., 2005; Nakahara et al., 1997). However, glutamate and ACPD mainly target the metabotropic glutamatergic receptor mGluR5 on astrocytes. In contrast, ATP is capable of activating both metabotropic (P2Y) and ionotropic (P2X) purinergic receptors, which may lead to a more complex dynamic of Ca^{2+} signaling. Astrocytes from both cultures also exhibited spontaneous $[Ca^{2+}]_i$ microdomains not associated with Ca^{2+} events in cell bodies and unlikely to be derived from the endoplasmic reticulum. The appearance of such $[Ca^{2+}]_i$ microdomains are consistent with recordings in brain tissue slices and in vivo studies, where spontaneous Ca^{2+} events localize only to astrocyte processes (Di Castro et al., 2011; Rungta et al., 2016; Shigetomi et al., 2013).

4.4 | Resting $[cAMP]_i$ level is higher in NB+ astrocytes, whereas the subcellular distribution of $[cAMP]_i$ is unchanged

Epac1-camps measurements revealed increased resting $[cAMP]_i$ in NB+ astrocytes (Figure 4), consistent with previous reports showing that increased $[cAMP]_i$ modulates arborization in astrocytes (Koyama et al., 1993; Schiweck et al., 2018; Vardjan et al., 2014; Won & Oh, 2000). Recent studies of subcellular heterogeneity in $[cAMP]_i$ consider that the activity of phosphodiesterase and protein kinase A

are the organizers of subcellular microdomains in $[cAMP]_i$ (Bock et al., 2020; Zhang et al., 2020). In our FRET-based studies of subcellular heterogeneity of $[cAMP]_i$, we first ruled out technical artifacts by demonstrating that the ratio of the fluorescence signal is independent from the subcellular amount of the fluorescent cAMP nanosensor (Figure S10). The results revealed that subcellular heterogeneity in $[cAMP]_i$ at rest and after NA stimulation was similar in both types of cultured astrocytes. Analysis of subcellular microdomains positioned in series along a line drawn from the nucleus toward the periphery revealed spatial inhomogeneity in $[cAMP]_i$ in 18% DMEM+ and in 35% NB+ resting astrocytes. After NA stimulation, the spatial inhomogeneity in $[cAMP]_i$ was measured in 27% DMEM+ and in 45% NB+ astrocytes (Figures 5 and 6; Table S3). However, the subcellular capacity for NA-evoked cAMP production (measured by the difference between the increased and resting cAMP levels in microdomains from the cell body toward the periphery/processes) increased in NB+, whereas it decreased in DMEM+ astrocytes (Figure 6d). The nature of this subcellular heterogeneity is unknown and awaits further studies. However, differences in the surface-to-volume ratio may lead to the formation of gradients in $[cAMP]_i$ between different parts of a cell, with higher $[cAMP]_i$ concentrations in finer structures (Neves et al., 2008) and spatial differences in the amount of molecular organizers of cAMP signaling (Bock et al., 2020; Zhang et al., 2020).

In summary, we have revealed that processes bearing arborized astrocytes associate with altered vesicle dynamics and increased subcellular heterogeneity in Ca^{2+} signaling but not in cAMP signaling. We conclude that cAMP signaling in astrocytes is less plastic than Ca^{2+} signaling, which merits further in vivo studies.

ACKNOWLEDGMENTS

The authors acknowledge financial support from the Slovenian Research Agency (SRA) research core funding #P3-0310, SRA projects #J3-2523, #J3-9266, #J3-7605, COST action CA18133 (ERNEST) and CipKeBip. The authors thank Prof. R. Jerala and Prof. M. Benčina from the National Institute of Chemistry for allowing us to use the EnSpire AlphaScreen technology system and Dr. S. Koren (Omega d.o.o.) for assisting measurements of cAMP accumulation, and Ms. D. Jošić for help with cell culturing and analysis.

CONFLICT OF INTEREST

The authors declare no conflict of interest.

DATA AVAILABILITY STATEMENT

The authors declare that the findings of this study are available in the article and in the supplementary material of this article. The data are available upon reasonable request from the corresponding authors.

ORCID

Nina Vardjan https://orcid.org/0000-0001-8174-1668
Robert Zorec https://orcid.org/0000-0002-7478-3875

REFERENCES

Alloisio, S., Cugnoli, C., Ferroni, S., & Nobile, M. (2004). Differential modulation of ATP-induced calcium signalling by A1 and A2 adenosine receptors in cultured cortical astrocytes. *British Journal of Pharmacology*, *141*(6), 935–942.

Araque, A., Parpura, V., Sanzgiri, R. P., & Haydon, P. G. (1999). Tripartite synapses: Glia, the unacknowledged partner. *Trends in Neurosciences*, *22*(5), 208–215.

Aswad, H., Jalabert, A., & Rome, S. (2016). Depleting extracellular vesicles from fetal bovine serum alters proliferation and differentiation of skeletal muscle cells in vitro. *BMC Biotechnology*, *16*, 32.

Attwell, D., Buchan, A. M., Charpak, S., Lauritzen, M., Macvicar, B. A., & Newman, E. A. (2010). Glial and neuronal control of brain blood flow. *Nature*, *468*(7321), 232–243.

Augusto-Oliveira, M., Arrifano, G. P., Takeda, P. Y., Lopes-Araujo, A., Santos-Sacramento, L., Anthony, D. C., Verkhratsky, A., & Crespo-Lopez, M. E. (2020). Astroglia-specific contributions to the regulation of synapses, cognition and behaviour. *Neuroscience and Biobehavioral Reviews*, *118*, 331–357.

Bartlett, P. J., Metzger, W., Gaspers, L. D., & Thomas, A. P. (2015). Differential regulation of multiple steps in inositol 1,4,5-trisphosphate signaling by protein kinase C shapes hormone-stimulated Ca2+ oscillations. *The Journal of Biological Chemistry*, *290*(30), 18519–18533.

Belanger, M., Allaman, I., & Magistretti, P. J. (2011). Brain energy metabolism: Focus on astrocyte-neuron metabolic cooperation. *Cell Metabolism*, *14*(6), 724–738.

Belanger, M., & Magistretti, P. J. (2009). The role of astroglia in neuroprotection. *Dialogues in Clinical Neuroscience*, *11*(3), 281–295.

Benediktsson, A. M., Schachtele, S. J., Green, S. H., & Dailey, M. E. (2005). Ballistic labeling and dynamic imaging of astrocytes in organotypic hippocampal slice cultures. *Journal of Neuroscience Methods*, *141*(1), 41–53.

Bernal, A., & Arranz, L. (2018). Nestin-expressing progenitor cells: Function, identity and therapeutic implications. *Cellular and Molecular Life Sciences*, *75*(12), 2177–2195.

Bock, A., Annibale, P., Konrad, C., Hannawacker, A., Anton, S. E., Maiellaro, I., Zabel, U., Sivaramakrishnan, S., Falcke, M., & Lohse, M. J. (2020). Optical mapping of cAMP signaling at the nanometer scale. *Cell*, *182*(6), 1519–1530 e17.

Borner, S., Schwede, F., Schlipp, A., Berisha, F., Calebiro, D., Lohse, M. J., & Nikolaev, V. O. (2011). FRET measurements of intracellular cAMP concentrations and cAMP analog permeability in intact cells. *Nature Protocols*, *6*(4), 427–438.

Bozic, M., Verkhratsky, A., Zorec, R., & Stenovec, M. (2020). Exocytosis of large-diameter lysosomes mediates interferon gamma-induced relocation of MHC class II molecules toward the surface of astrocytes. *Cellular and Molecular Life Sciences*, *77*(16), 3245–3264.

Bushong, E. A., Martone, M. E., & Ellisman, M. H. (2004). Maturation of astrocyte morphology and the establishment of astrocyte domains during postnatal hippocampal development. *International Journal of Developmental Neuroscience*, *22*(2), 73–86.

Chung, W. S., Allen, N. J., & Eroglu, C. (2015). Astrocytes control synapse formation, function, and elimination. *Cold Spring Harbor Perspectives in Biology*, *7*(9), a020370.

Codeluppi, S., Gregory, E. N., Kjell, J., Wigerblad, G., Olson, L., & Svensson, C. I. (2011). Influence of rat substrain and growth conditions on the characteristics of primary cultures of adult rat spinal cord astrocytes. *Journal of Neuroscience Methods*, *197*(1), 118–127.

Connor, J. R., & Berkowitz, E. M. (1985). A demonstration of glial filament distribution in astrocytes isolated from rat cerebral cortex. *Neuroscience*, *16*(1), 33–44.

Crippa, D., Schenk, U., Francolini, M., Rosa, P., Verderio, C., Zonta, M., Pozzan, T., Matteoli, M., & Carmignoto, G. (2006). Synaptobrevin2-expressing vesicles in rat astrocytes: Insights into molecular characterization, dynamics and exocytosis. *The Journal of Physiology*, *570*(Pt 3), 567–582.

D'Adamo, P., Horvat, A., Gurgone, A., Mignogna, M. L., Bianchi, V., Masetti, M., Ripamonti, M., Taverna, S., Velebit, J., Malnar, M., &

others. (2021). Inhibiting glycolysis rescues memory impairment in an intellectual disability Gdi1-null mouse. *Metabolism*, *116*, 154463.

Dallwig, R., & Deitmer, J. W. (2002). Cell-type specific calcium responses in acute rat hippocampal slices. *Journal of Neuroscience Methods*, *116* (1), 77–87.

Dawitz, J., Kroon, T., Hjorth, J. J., & Meredith, R. M. (2011). Functional calcium imaging in developing cortical networks. *Journal of Visualized Experiments*, *56*, 1–8. https://doi.org/10.3791/35501

De Pitta, M., Goldberg, M., Volman, V., Berry, H., & Ben-Jacob, E. (2009). Glutamate regulation of calcium and IP3 oscillating and pulsating dynamics in astrocytes. *Journal of Biological Physics*, *35*(4), 383–411.

Di Castro, M. A., Chuquet, J., Liaudet, N., Bhaukaurally, K., Santello, M., Bouvier, D., Tiret, P., & Volterra, A. (2011). Local Ca2+ detection and modulation of synaptic release by astrocytes. *Nature Neuroscience*, *14* (10), 1276–1284.

Dong, T. X., Othy, S., Jairaman, A., Skupsky, J., Zavala, A., Parker, I., Dynes, J. L., & Cahalan, M. D. (2017). T-cell calcium dynamics visualized in a ratiometric tdTomato-GCaMP6f transgenic reporter mouse. *eLife*, *6*, e32417. https://doi.org/10.7554/eLife.32417

Du, F., Qian, Z. M., Zhu, L., Wu, X. M., Qian, C., Chan, R., & Ke, Y. (2010). Purity, cell viability, expression of GFAP and bystin in astrocytes cultured by different procedures. *Journal of Cellular Biochemistry*, *109*(1), 30–37.

Escartin, C., Galea, E., Lakatos, A., O'Callaghan, J. P., Petzold, G. C., Serrano-Pozo, A., Steinhauser, C., Volterra, A., Carmignoto, G., Agarwal, A., & others. (2021). Reactive astrocyte nomenclature, definitions, and future directions. *Nature Neuroscience*, *24*(3), 312–325.

Fischer, G., Leutz, A., & Schachner, M. (1982). Cultivation of immature astrocytes of mouse cerebellum in a serum-free, hormonally defined medium. Appearance of the mature astrocyte phenotype after addition of serum. *Neuroscience Letters*, *29*(3), 297–302.

Foo, L. C., Allen, N. J., Bushong, E. A., Ventura, P. B., Chung, W. S., Zhou, L., Cahoy, J. D., Daneman, R., Zong, H., Ellisman, M. H., & Barres, B. A. (2011). Development of a method for the purification and culture of rodent astrocytes. *Neuron*, *71*(5), 799–811.

Goncalves, P. P., Stenovec, M., Chowdhury, H. H., Grilc, S., Kreft, M., & Zorec, R. (2008). Prolactin secretion sites contain syntaxin-1 and differ from ganglioside monosialic acid rafts in rat lactotrophs. *Endocrinology*, *149*(10), 4948–4957.

Grynkiewicz, G., Poenie, M., & Tsien, R. Y. (1985). A new generation of Ca2+ indicators with greatly improved fluorescence properties. *The Journal of Biological Chemistry*, *260*(6), 3440–3450.

Gucek, A., Jorgacevski, J., Singh, P., Geisler, C., Lisjak, M., Vardjan, N., Kreft, M., Egner, A., & Zorec, R. (2016). Dominant negative SNARE peptides stabilize the fusion pore in a narrow, release-unproductive state. *Cellular and Molecular Life Sciences*, *73*(19), 3719–3731.

Harang, R., Bonnet, G., & Petzold, L. R. (2012). WAVOS: A MATLAB toolkit for wavelet analysis and visualization of oscillatory systems. *BMC Research Notes*, *5*, 163.

Henkel, A. W., Meiri, H., Horstmann, H., Lindau, M., & Almers, W. (2000). Rhythmic opening and closing of vesicles during constitutive exo- and endocytosis in chromaffin cells. *The EMBO Journal*, *19*(1), 84–93.

Hirase, H., Qian, L., Barthó, P., & Buzsáki, G. (2004). Calcium dynamics of cortical astrocytic networks in vivo. *PLoS Biology*, *2*(4), e96.

Horvat, A., & Vardjan, N. (2019). Astroglial cAMP signalling in space and time. *Neuroscience Letters*, *689*, 5–10.

Horvat, A., Zorec, R., & Vardjan, N. (2016). Adrenergic stimulation of single rat astrocytes results in distinct temporal changes in intracellular ca(2+) and cAMP-dependent PKA responses. *Cell Calcium*, *59*(4), 156–163.

Jayme, D., Watanabe, T., & Shimada, T. (1997). Basal medium development for serum-free culture: A historical perspective. *Cytotechnology*, *23*(1–3), 95–101.

John, G. R., Chen, L., Rivieccio, M. A., Melendez-Vasquez, C. V., Hartley, A., & Brosnan, C. F. (2004). Interleukin-1beta induces a reactive astroglial phenotype via deactivation of the rho GTPase-Rock axis. *The Journal of Neuroscience*, *24*(11), 2837–2845.

Kabaso, D., Jorgacevski, J., Calejo, A. I., Flasker, A., Gucek, A., Kreft, M., & Zorec, R. (2013). Comparison of unitary exocytic events in pituitary lactotrophs and in astrocytes: Modeling the discrete open fusion-pore states. *Frontiers in Cellular Neuroscience*, *7*, 33.

Kim R, Healey KL, Sepulveda-Orengo MT, Reissner KJ. 2018. Astroglial correlates of neuropsychiatric disease: From astrocytopathy to astrogliosis. *Progress in Neuropsychopharmacology and Biological Psychiatry 87*(Pt A):126-146.

Koyama, Y., Ishibashi, T., Hayata, K., & Baba, A. (1993). Endothelins modulate dibutyryl cAMP-induced stellation of cultured astrocytes. *Brain Research*, *600*(1), 81–88.

Kreft, M., & Zorec, R. (1997). Cell-attached measurements of attofarad capacitance steps in rat melanotrophs. *Pflügers Archiv*, *434*(2), 212–214.

Lasič, E., Lisjak, M., Horvat, A., Božić, M., Šakanović, A., Anderluh, G., Verkhratsky, A., Vardjan, N., Jorgačevski, J., Stenovec, M., & Zorec, R. (2019). Astrocyte specific remodeling of Plasmalemmal cholesterol composition by ketamine indicates a new mechanism of antidepressant action. *Scientific Reports*, *9*(1), 10957.

Lasic, E., Rituper, B., Jorgacevski, J., Kreft, M., Stenovec, M., & Zorec, R. (2016). Subanesthetic doses of ketamine stabilize the fusion pore in a narrow flickering state in astrocytes. *Journal of Neurochemistry*, *138*(6), 909–917.

Lasic, E., Stenovec, M., Kreft, M., Robinson, P. J., & Zorec, R. (2017). Dynamin regulates the fusion pore of endo- and exocytotic vesicles as revealed by membrane capacitance measurements. *Biochimica et Biophysica Acta*, *1861*(9), 2293–2303. https://doi.org/10.1016/j.bbagen.2017.06.0229

Lasic, E., Trkov Bobnar, S., Wilhelmsson, U., de Pablo, Y., Pekny, M., Zorec, R., & Stenovec, M. (2020). Nestin affects fusion pore dynamics in mouse astrocytes. *Acta Physiologica (Oxford, England)*, *228*(3), e13399.

Lindau, M. (1991). Time-resolved capacitance measurements: Monitoring exocytosis in single cells. *Quarterly Reviews of Biophysics*, *24*(1), 75–101.

McCarthy, K. D., & de Vellis, J. (1980). Preparation of separate astroglial and oligodendroglial cell cultures from rat cerebral tissue. *The Journal of Cell Biology*, *85*(3), 890–902.

Messam, C. A., Hou, J., & Major, E. O. (2000). Coexpression of nestin in neural and glial cells in the developing human CNS defined by a human-specific anti-nestin antibody. *Experimental Neurology*, *161*(2), 585–596.

Mikolajewicz, N., Smith, D., Komarova, S. V., & Khadra, A. (2021). High-affinity P2Y2 and low-affinity P2X7 receptor interaction modulates ATP-mediated calcium signaling in murine osteoblasts. *PLoS Computational Biology*, *17*(6), e1008872.

Morita, M., Higuchi, C., Moto, T., Kozuka, N., Susuki, J., Itofusa, R., Yamashita, J., & Kudo, Y. (2003). Dual regulation of calcium oscillation in astrocytes by growth factors and pro-inflammatory cytokines via the mitogen-activated protein kinase cascade. *The Journal of Neuroscience*, *23*(34), 10944–10952.

Morita, M., Kozuka, N., Itofusa, R., Yukawa, M., & Kudo, Y. (2005). Autocrine activation of EGF receptor promotes oscillation of glutamate-induced calcium increase in astrocytes cultured in rat cerebral cortex. *Journal of Neurochemistry*, *95*(3), 871–879.

Morita, M., & Kudo, Y. (2010). Growth factors upregulate astrocyte [Ca2+]i oscillation by increasing SERCA2b expression. *Glia*, *58*(16), 1988–1995.

Morita, M., Nakane, A., Fujii, Y., Maekawa, S., & Kudo, Y. (2015). High cell density upregulates calcium oscillation by increasing calcium store content via basal mitogen-activated protein kinase activity. *PLoS One*, *10*(9), e0137610.

Morita, M., Nakane, A., Maekawa, S., & Kudo, Y. (2015). Pharmacological characterization of the involvement of protein kinase C in oscillatory and non-oscillatory calcium increases in astrocytes. *Journal of Pharmacological Sciences*, *129*(1), 38–42.

Morrison, R. S., & de Vellis, J. (1981). Growth of purified astrocytes in a chemically defined medium. *Proceedings of the National Academy of Sciences of the United States of America*, *78*(11), 7205–7209.

Murk, K., Blanco Suarez, E. M., Cockbill, L. M., Banks, P., & Hanley, J. G. (2013). The antagonistic modulation of Arp2/3 activity by N-WASP, WAVE2 and PICK1 defines dynamic changes in astrocyte morphology. *Journal of Cell Science*, *126*(Pt 17), 3873–3883.

Nakahara, K., Okada, M., & Nakanishi, S. (1997). The metabotropic glutamate receptor mGluR5 induces calcium oscillations in cultured astrocytes via protein kinase C phosphorylation. *Journal of Neurochemistry*, *69*(4), 1467–1475.

Nash, M. S., Schell, M. J., Atkinson, P. J., Johnston, N. R., Nahorski, S. R., & Challiss, R. A. (2002). Determinants of metabotropic glutamate receptor-5-mediated Ca2+ and inositol 1,4,5-trisphosphate oscillation frequency. Receptor density versus agonist concentration. *The Journal of Biological Chemistry*, *277*(39), 35947–35960.

Neher, E., & Marty, A. (1982). Discrete changes of cell membrane capacitance observed under conditions of enhanced secretion in bovine adrenal chromaffin cells. *Proceedings of the National Academy of Sciences of the United States of America*, *79*(21), 6712–6716.

Nett, W. J., Oloff, S. H., & McCarthy, K. D. (2002). Hippocampal astrocytes in situ exhibit calcium oscillations that occur independent of neuronal activity. *Journal of Neurophysiology*, *87*(1), 528–537.

Neves, S. R., Tsokas, P., Sarkar, A., Grace, E. A., Rangamani, P., Taubenfeld, S. M., Alberini, C. M., Schaff, J. C., Blitzer, R. D., Moraru, I. I., & Iyengar, R. (2008). Cell shape and negative links in regulatory motifs together control spatial information flow in signaling networks. *Cell*, *133*(4), 666–680.

Nikolaev, V. O., Bunemann, M., Hein, L., Hannawacker, A., & Lohse, M. J. (2004). Novel single chain cAMP sensors for receptor-induced signal propagation. *Journal of Biological Chemistry*, *279*(36), 37215–37218.

Nimmerjahn, A., Kirchhoff, F., Kerr, J. N., & Helmchen, F. (2004). Sulforhodamine 101 as a specific marker of astroglia in the neocortex in vivo. *Nature Methods*, *1*(1), 31–37. https://doi.org/10.1038/nmeth706

Nobile, M., Monaldi, I., Alloisio, S., Cugnoli, C., & Ferroni, S. (2003). ATP-induced, sustained calcium signalling in cultured rat cortical astrocytes: Evidence for a non-capacitative, P2X7-like-mediated calcium entry. *FEBS Letters*, *538*(1–3), 71–76.

O'Shea, R. D., Lau, C. L., Zulaziz, N., Maclean, F. L., Nisbet, D. R., Horne, M. K., & Beart, P. M. (2015). Transcriptomic analysis and 3D bioengineering of astrocytes indicate ROCK inhibition produces cytotrophic astrogliosis. *Frontiers in Neuroscience*, *9*, 50.

Oe, Y., Wang, X., Patriarchi, T., Konno, A., Ozawa, K., Yahagi, K., Hirai, H., Tsuboi, T., Kitaguchi, T., Tian, L., Mc Hugh, T., & Hirase, H. (2020). Distinct temporal integration of noradrenaline signaling by astrocytic second messengers during vigilance. *Nature Communications*, *11*(1), 471.

Paco, S., Hummel, M., Pla, V., Sumoy, L., & Aguado, F. (2016). Cyclic AMP signaling restricts activation and promotes maturation and antioxidant defenses in astrocytes. *BMC Genomics*, *17*, 304.

Pangrsic, T., Potokar, M., Haydon, P. G., Zorec, R., & Kreft, M. (2006). Astrocyte swelling leads to membrane unfolding, not membrane insertion. *Journal of Neurochemistry*, *99*(2), 514–523.

Pasti, L., Pozzan, T., & Carmignoto, G. (1995). Long-lasting changes of calcium oscillations in astrocytes. A new form of glutamate-mediated plasticity. *The Journal of Biological Chemistry*, *270*(25), 15203–15210.

Pekny, M., Pekna, M., Messing, A., Steinhauser, C., Lee, J. M., Parpura, V., Hol, E. M., Sofroniew, M. V., & Verkhratsky, A. (2016). Astrocytes: A central element in neurological diseases. *Acta Neuropathologica*, *131*(3), 323–345.

Piazza, V., Ciubotaru, C. D., Gale, J. E., & Mammano, F. (2007). Purinergic signalling and intercellular Ca2+ wave propagation in the organ of Corti. *Cell Calcium*, *41*(1), 77–86.

Placone, A. L., McGuiggan, P. M., Bergles, D. E., Guerrero-Cazares, H., Quinones-Hinojosa, A., & Searson, P. C. (2015). Human astrocytes develop physiological morphology and remain quiescent in a novel 3D matrix. *Biomaterials*, *42*, 134–143.

Potokar, M., Kreft, M., Li, L., Daniel Andersson, J., Pangrsic, T., Chowdhury, H. H., Pekny, M., & Zorec, R. (2007). Cytoskeleton and vesicle mobility in astrocytes. *Traffic*, *8*(1), 12–20.

Potokar, M., Stenovec, M., Kreft, M., Kreft, M. E., & Zorec, R. (2008). Stimulation inhibits the mobility of recycling peptidergic vesicles in astrocytes. *Glia*, *56*(2), 135–144.

Potokar, M., Vardjan, N., Stenovec, M., Gabrijel, M., Trkov, S., Jorgačevski, J., Kreft, M., & Zorec, R. (2013). Astrocytic vesicle mobility in health and disease. *International Journal of Molecular Sciences*, *14*(6), 11238–11258.

Puschmann, T. B., Zanden, C., De Pablo, Y., Kirchhoff, F., Pekna, M., Liu, J., & Pekny, M. (2013). Bioactive 3D cell culture system minimizes cellular stress and maintains the in vivo-like morphological complexity of astroglial cells. *Glia*, *61*(3), 432–440.

Puschmann, T. B., Zanden, C., Lebkuechner, I., Philippot, C., de Pablo, Y., Liu, J., & Pekny, M. (2014). HB-EGF affects astrocyte morphology, proliferation, differentiation, and the expression of intermediate filament proteins. *Journal of Neurochemistry*, *128*(6), 878–889.

Racchetti, G., D'Alessandro, R., & Meldolesi, J. (2012). Astrocyte stellation, a process dependent on Rac1 is sustained by the regulated exocytosis of enlargeosomes. *Glia*, *60*(3), 465–475.

Rigal, A., Doyle, S. M., & Robert, S. (2015). Live cell imaging of FM4-64, a tool for tracing the endocytic pathways in Arabidopsis root cells. *Methods in Molecular Biology*, *1242*, 93–103.

Rituper, B., Gucek, A., Jorgacevski, J., Flasker, A., Kreft, M., & Zorec, R. (2013). High-resolution membrane capacitance measurements for the study of exocytosis and endocytosis. *Nature Protocols*, *8*(6), 1169–1183.

Rungta, R. L., Bernier, L. P., Dissing-Olesen, L., Groten, C. J., LeDue, J. M., Ko, R., Drissler, S., & MacVicar, B. A. (2016). Ca(2+) transients in astrocyte fine processes occur via ca(2+) influx in the adult mouse hippocampus. *Glia*, *64*(12), 2093–2103.

Schachtrup, C., Ryu, J. K., Helmrick, M. J., Vagena, E., Galanakis, D. K., Degen, J. L., Margolis, R. U., & Akassoglou, K. (2010). Fibrinogen triggers astrocyte scar formation by promoting the availability of active TGF-beta after vascular damage. *The Journal of Neuroscience*, *30*(17), 5843–5854.

Schiweck, J., Eickholt, B. J., & Murk, K. (2018). Important shapeshifter: Mechanisms allowing astrocytes to respond to the changing nervous system during development, injury and disease. *Frontiers in Cellular Neuroscience*, *12*, 261.

Schwartz, J. P., & Wilson, D. J. (1992). Preparation and characterization of type 1 astrocytes cultured from adult rat cortex, cerebellum, and striatum. *Glia*, *5*(1), 75–80.

Shigetomi, E., Bushong, E. A., Haustein, M. D., Tong, X., Jackson-Weaver, O., Kracun, S., Xu, J., Sofroniew, M. V., Ellisman, M. H., & Khakh, B. S. (2013). Imaging calcium microdomains within entire astrocyte territories and endfeet with GCaMPs expressed using adeno-associated viruses. *The Journal of General Physiology*, *141*(5), 633–647.

Sofroniew, M. V. (2009). Molecular dissection of reactive astrogliosis and glial scar formation. *Trends in Neurosciences*, *32*(12), 638–647.

Spruce, A. E., Breckenridge, L. J., Lee, A. K., & Almers, W. (1990). Properties of the fusion pore that forms during exocytosis of a mast cell secretory vesicle. *Neuron*, *4*(5), 643–654.

Stenovec, M., Lasič, E., Božić, M., Bobnar, S. T., Stout, R. F., Grubišić, V., Parpura, V., & Zorec, R. (2016). Ketamine inhibits ATP-evoked Exocytotic release of brain-derived neurotrophic factor from vesicles in cultured rat astrocytes. *Molecular Neurobiology*, *53*(10), 6882–6896.

Stenovec, M., Li, B., Verkhratsky, A., & Zorec, R. (2020). Astrocytes in rapid ketamine antidepressant action. *Neuropharmacology*, *173*, 108158.

Sudhof, T. C. (2012). Calcium control of neurotransmitter release. *Cold Spring Harbor Perspectives in Biology*, *4*(1), a011353.

Szekely, D., Brennan, S. C., Mun, H. C., Conigrave, A. D., & Kuchel, P. W. (2009). Effectors of the frequency of calcium oscillations in HEK-293 cells: Wavelet analysis and a computer model. *European Biophysics Journal*, *39*(1), 149–165.

Trachtenberg, M. C., Kornblith, P. L., & Hauptli, J. (1972). Biophysical properties of cultured human glial cells. *Brain Research*, *38*(2), 279–298.

Vardjan, N., Horvat, A., Anderson, J. E., Yu, D., Croom, D., Zeng, X., Lužnik, Z., Kreft, M., Teng, Y. D., Kirov, S. A., & Zorec, R. (2016). Adrenergic activation attenuates astrocyte swelling induced by hypotonicity and neurotrauma. *Glia*, *64*(6), 1034–1049.

Vardjan, N., Kreft, M., & Zorec, R. (2014). Dynamics of β-adrenergic/cAMP signaling and morphological changes in cultured astrocytes. *Glia*, *62*(4), 566–579.

Vardjan, N., & Zorec, R. (2015). Excitable astrocytes: Ca(2+)- and cAMP-regulated exocytosis. *Neurochemical Research*, *40*(12), 2414–2414.

Verkhratsky, A., Matteoli, M., Parpura, V., Mothet, J. P., & Zorec, R. (2016). Astrocytes as secretory cells of the central nervous system: Idiosyncrasies of vesicular secretion. *The EMBO Journal*, *35*(3), 239–257.

Verkhratsky, A., & Nedergaard, M. (2018). Physiology of Astroglia. *Physiological Reviews*, *98*(1), 239–389.

Verkhratsky, A., Rodrigues, J. J., Pivoriunas, A., Zorec, R., & Semyanov, A. (2019). Astroglial atrophy in Alzheimer's disease. *Pflügers Archiv*, *471*(10), 1247–1261.

Verkhratsky, A., Rodriguez, J. J., & Steardo, L. (2014). Astrogliopathology: A central element of neuropsychiatric diseases? *Neuroscientist*, *20*(6), 576–588.

Verkhratsky, A., Semyanov, A., & Zorec, R. (2020). Physiology of Astroglial excitability. *Function*, *1*(2), 1–15. https://doi.org/10.1093/function/zqaa016

Verkhratsky, A., Zorec, R., & Parpura, V. (2017). Stratification of astrocytes in healthy and diseased brain. *Brain Pathology*, *27*(5), 629–644.

Wolfes, A. C., Ahmed, S., Awasthi, A., Stahlberg, M. A., Rajput, A., Magruder, D. S., Bonn, S., & Dean, C. (2017). A novel method for culturing stellate astrocytes reveals spatially distinct Ca2+ signaling and vesicle recycling in astrocytic processes. *Journal of General Physiology*, *149*(1), 149–170.

Wolfes, A. C., & Dean, C. (2018). Culturing in vivo-like murine astrocytes using the fast, simple, and inexpensive AWESAM protocol. *Journal of Visualized Experiments*, *131*.1–7. https://doi.org/10.3791/56092

Won, C. L., & Oh, Y. S. (2000). cAMP-induced stellation in primary astrocyte cultures with regional heterogeneity. *Brain Research*, *887*(2), 250–258.

Yang, Z., & Wang, K. K. (2015). Glial fibrillary acidic protein: From intermediate filament assembly and gliosis to neurobiomarker. *Trends in Neurosciences*, *38*(6), 364–374.

Yoshida, Y., Tsuchiya, R., Matsumoto, N., Morita, M., Miyakawa, H., & Kudo, Y. (2005). Ca2+−dependent induction of intracellular Ca2+ oscillation in hippocampal astrocytes during metabotropic glutamate receptor activation. *Journal of Pharmacological Sciences*, *97*(2), 212–218.

Zamanian, J. L., Xu, L., Foo, L. C., Nouri, N., Zhou, L., Giffard, R. G., & Barres, B. A. (2012). Genomic analysis of reactive astrogliosis. *Journal of Neuroscience*, *32*(18), 6391–6410.

Zeisel, A., Hochgerner, H., Lönnerberg, P., Johnsson, A., Memic, F., van der Zwan, J., Häring, M., Braun, E., Borm, L. E., la Manno, G., Codeluppi, S., Furlan, A., Lee, K., Skene, N., Harris, K. D., Hjerling-Leffler, J., Arenas, E., Ernfors, P., Marklund, U., & Linnarsson, S. (2018). Molecular architecture of the mouse nervous system. *Cell*, *174*(4), 999–1014.e22.

Zhang, J. Z., Lu, T. W., Stolerman, L. M., Tenner, B., Yang, J. R., Zhang, J. F., Falcke, M., Rangamani, P., Taylor, S. S., Mehta, S., & Zhang, J. (2020). Phase separation of a PKA regulatory subunit controls cAMP compartmentation and oncogenic signaling. *Cell*, *182*(6), 1531–1544.e15.

Zhang, Q., Fukuda, M., Van Bockstaele, E., Pascual, O., & Haydon, P. G. (2004). Synaptotagmin IV regulates glial glutamate release. *Proceedings of the National Academy of Sciences of the United States of America*, *101*(25), 9441–9446.

Zhang, Y., Sloan, S. A., Clarke, L. E., Caneda, C., Plaza, C. A., Blumenthal, P. D., Vogel, H., Steinberg, G. K., Edwards, M. S., Li, G., Duncan, J. A., 3rd, Cheshier, S. H., Shuer, L. M., Chang, E. F., Grant, G. A., Gephart, M. G., & Barres, B. A. (2016). Purification and characterization of progenitor and mature human astrocytes reveals transcriptional and functional differences with mouse. *Neuron*, *89*(1), 37–53.

Zhang, Z., Bhalla, A., Dean, C., Chapman, E. R., & Jackson, M. B. (2009). Synaptotagmin IV: A multifunctional regulator of peptidergic nerve terminals. *Nature Neuroscience*, *12*(2), 163–171.

Zheng, X., Baker, H., Hancock, W. S., Fawaz, F., McCaman, M., & Pungor, E., Jr. (2006). Proteomic analysis for the assessment of different lots of fetal bovine serum as a raw material for cell culture. Part IV. Application of proteomics to the manufacture of biological drugs. *Biotechnology Progress*, *22*(5), 1294–1300.

Zorec, R., Horvat, A., Vardjan, N., & Verkhratsky, A. (2015). Memory formation shaped by Astroglia. *Frontiers in Integrative Neuroscience*, *9*, 56.

Zorec, R., Sikdar, S. K., & Mason, W. T. (1991). Increased cytosolic calcium stimulates exocytosis in bovine lactotrophs. Direct evidence from changes in membrane capacitance. *Journal of General Physiology*, *97*(3), 473–497.

SUPPORTING INFORMATION

Additional supporting information may be found in the online version of the article at the publisher's website.

How to cite this article: Pirnat, S., Božić, M., Dolanc, D., Horvat, A., Tavčar, P., Vardjan, N., Verkhratsky, A., Zorec, R., & Stenovec, M. (2021). Astrocyte arborization enhances Ca^{2+} but not cAMP signaling plasticity. *Glia*, *69*(12), 2899–2916. https://doi.org/10.1002/glia.24076